



Measurement of prompt charged-particle production in pp collisions at $\sqrt{s} = 13$ TeV

LHCb collaboration[†]

Abstract

The differential cross-section of prompt inclusive production of long-lived charged particles in proton-proton collisions is measured using a data sample recorded by the LHCb experiment at a centre-of-mass energy of $\sqrt{s} = 13$ TeV. The data sample, collected with an unbiased trigger, corresponds to an integrated luminosity of 5.4 nb^{-1} . The differential cross-section is measured as a function of transverse momentum and pseudorapidity in the ranges $p_T \in [0.08, 10) \text{ GeV}/c$ and $\eta \in [2.0, 4.8)$ and is determined separately for positively and negatively charged particles. The results are compared with predictions from various hadronic-interaction models.

Submitted to JHEP

© 2022 CERN for the benefit of the LHCb collaboration. CC BY 4.0 licence.

[†]Authors are listed at the end of this paper.

1 Introduction

Hadron production in inelastic high-energy proton-proton (pp) collisions is dominated by soft processes of quantum chromodynamics (QCD). Most of the hadron production cannot be calculated from first principles in perturbative QCD due to the small average momentum transfer. Instead, predictions are based on phenomenological models. The determination of their parameters relies on input from experiments. Monte Carlo event generators, in which these models are implemented, are used at the Large Hadron Collider (LHC) to simulate the final-state particles originating from the soft component of a collision. An introduction to soft-QCD theories is presented in Refs. [1–5].

In the field of cosmic-ray research, generators are employed to simulate interactions of ultra-relativistic nuclei with the atmosphere of the Earth, which induce extensive particle cascades, referred to as air showers. Although often used to predict interactions in a phase space that is not covered by the input from experiments, the generators are remarkably successful at describing many features of air showers. However, a long-standing excess is observed in the number of muons produced in high-energy air showers compared to simulations, termed the Muon Puzzle [6, 7]. Measurements of the production of light hadrons in the forward region are needed to further guide and constrain the models [8–10]. Since the LHCb detector covers the forward pseudorapidity range, studies performed in its acceptance are of particular interest for cosmic-ray research.

A suitable proxy for the prompt production of light hadrons is the production of prompt charged long-lived particles. Precision measurements of prompt charged-particle production in collisions at the TeV energy scale are needed to validate and tune the hadronic-interaction models and to safely extrapolate them to even higher collision energies that are of interest in astroparticle physics. This tuning results in a more accurate simulation, which is essential, *e.g.*, in searches for physics beyond the Standard Model. These measurements specifically address the question whether the pseudorapidity distributions of hadrons are narrow or wide [10]. Approaches based on Gribov-Regge field theory model soft and hard Pomeron interactions. In the approach used by SIBYLL 2.3d [11] and DPMJET III [12, 13], the two regimes are rather decoupled and the pseudorapidity distribution is narrow, while the approach used by EPOS-LHC [14] and QGSJET II-04 [15] produces wider distributions.

In this paper, a measurement of the differential cross-section of inclusive production of prompt long-lived charged particles, *i.e.* primarily of pions, kaons and protons, in pp collisions is presented. The data sample was recorded by the LHCb experiment at a centre-of-mass energy of $\sqrt{s} = 13$ TeV in 2015 and corresponds to an integrated luminosity of 5.4 nb^{-1} . The differential cross-section is measured as a function of transverse momentum and pseudorapidity in the ranges $p_T \in [0.08, 10.00) \text{ GeV}/c$ and $\eta \in [2.0, 4.8)$ and is determined separately for positively and negatively charged particles. Both the charge-combined differential cross-section and the ratio of the differential cross-sections for the two charges are compared with predictions from four different hadronic-interaction models.

The paper is structured as follows. In Sect. 2, the detector as well as the data and simulated samples used in this measurement are described. The analysis strategy is presented in Sect. 3. The efficiencies and the background contributions are detailed in Sects. 4 and 5, respectively. In Sect. 6, the results are discussed, and a summary is provided in Sect. 7.

2 Detector and data sample

The LHCb detector [16, 17] is a single-arm forward spectrometer covering the pseudorapidity range $2 < \eta < 5$, designed for the study of particles containing b or c quarks. The detector includes a high-precision tracking system consisting of a silicon-strip vertex detector surrounding the pp interaction region, a large-area silicon-strip detector located upstream of a dipole magnet with a bending power of about 4 Tm, and three stations of silicon-strip detectors and straw drift tubes placed downstream of the magnet. The tracking system provides a measurement of the momentum, p , of charged particles with a relative uncertainty that varies from 0.5% at low momentum to 1.0% at 200 GeV/ c . The minimum distance of a track to a primary pp collision vertex, the impact parameter, is measured with a resolution of $(15 + 29/p_T) \mu\text{m}$, where p_T is the component of the momentum transverse to the beam, in GeV/ c . Different types of charged hadrons are distinguished using information from two ring-imaging Cherenkov detectors. Photons, electrons and hadrons are identified by a calorimeter system consisting of scintillating-pad and preshower detectors, an electromagnetic and a hadronic calorimeter. Muons are identified by a system composed of alternating layers of iron and multiwire proportional chambers.

The online event selection for this measurement is performed by an unbiased trigger. Therefore, no trigger-related systematic uncertainty arises. At the hardware stage, events are accepted at a fixed rate. The software stage then restricts the data sample to collisions of leading bunches of the LHC bunch trains, which avoids background from previous events, while the bunch spacing of 50 ns in these low-intensity runs avoids contributions to the read-out from following events. The analysed data sample contains the events from two LHC fills, recorded with opposite magnetic-field configurations of the LHCb dipole magnet. The field configuration that bends positively (negatively) charged particles in the horizontal plane towards the centre of the LHC ring is referred to as upwards (downwards). The fill recorded with the magnetic field pointing upwards comprises 226×10^6 events and corresponds to an integrated luminosity of 3.0 nb^{-1} , while the fill recorded with the magnetic field pointing downwards comprises 134×10^6 events and corresponds to an integrated luminosity of 2.4 nb^{-1} . The average numbers of collisions in a bunch crossing are 0.9 and 0.7 for these two fills, respectively. The results are obtained from the combined data sample, but as a cross-check, the analysis is also performed separately for each fill. To measure the background from interactions of the beams with residual gas in the beam pipe, beam-gas collisions are used, where only one of the two beams traverses the detector. Such collisions were also collected for each fill.

Simulation is required to model the effects of the imposed selection requirements and to study the background contributions. In the simulation, pp collisions are generated using PYTHIA [18] with a specific LHCb configuration [19]. Decays of unstable particles are described by EVTGEN [20], in which final-state radiation is generated using PHOTOS [21]. The interaction of the generated particles with the detector, and its response, are implemented using the GEANT4 toolkit [22] as described in Ref. [23]. For each of the two magnetic-field configurations, a trigger-unbiased sample containing 10^7 events was simulated.

3 Analysis strategy

Based on a particle count, n , in a pseudorapidity interval with a width of $\Delta\eta$ and a transverse-momentum interval with a width of Δp_T that is obtained from a data set corresponding to an integrated luminosity of \mathcal{L} , the differential cross-section is determined as

$$\frac{d^2\sigma}{d\eta dp_T} \equiv \frac{n}{\mathcal{L} \Delta\eta \Delta p_T}. \quad (1)$$

It is computed in finite intervals. The signal in this analysis is the number of prompt long-lived charged particles produced in beam-beam collisions. A particle is classified as a long-lived particle if its lifetime is greater than 30 ps, and prompt if it is produced directly in the primary interaction or if none of its ancestor particles is long-lived [24]. Long-lived charged particles are electrons, muons, pions, kaons and protons as well as Σ^+ , Σ^- , Ξ^- and Ω^- baryons and their antiparticles.

Tracks that traverse the entire tracking system are selected as candidates for prompt long-lived charged particles. Among these tracks, some are fakes. One type of fake tracks does not correspond to any real particle. Their contribution is reduced by imposing a requirement on the fake-track probability, provided by a neural-network-based algorithm [25], but the remaining contribution is still non-negligible. The second type of fake tracks occurs when two or more tracks are reconstructed for one real particle. Their contribution is suppressed below the level of 0.1 % in all kinematic intervals by the reconstruction software, and is negligible in this analysis. Non-prompt tracks passing the selection are another source of background. These tracks originate from interactions of particles with the detector material, interactions of the beams with residual gas or from decays of long-lived particles.

Consequently, the number of candidate tracks, n_{cand} , is related to the number of signal particles, n , according to

$$n_{\text{cand}} = \varepsilon n + \sum_i n_i, \quad (2)$$

where ε denotes the total efficiency, *i.e.* the product of the geometric acceptance of the detector, the track-reconstruction efficiency and the selection efficiency, and the sum includes the numbers of background tracks, n_i , from source i . The values of ε and n_i are taken from simulation. To correct for imperfect modelling, control measurements are performed, and the simulation is adjusted. For this purpose, observables, \mathcal{P}_i , that are proportional to n_i are chosen as proxies. The proxies for different sources of background are described in Sect. 5. The ratio of the background counts in data and simulation is assumed to be equal to the ratio of the proxies in data and simulation,

$$\frac{n_i}{n_{i,\text{sim}}} = \frac{\mathcal{P}_i}{\mathcal{P}_{i,\text{sim}}} \equiv R_i, \quad (3)$$

which allows the background count in data to be estimated as $n_i = R_i n_{i,\text{sim}}$.

The background induced by beam-gas interactions, which are not simulated, is determined from the number of candidate tracks, n_{gas} , produced in the recorded beam-gas events. Both the configuration where the beam travels from the vertex detector towards the muon system and the opposite configuration are included. The contributions from these configurations are scaled to the corresponding number of recorded beam-beam events.

In summary, the number of signal particles in Eq. (1) can be expressed as

$$n = \frac{1}{R_\epsilon \epsilon_{\text{sim}}} \left(n_{\text{cand}} - \sum_i R_i n_{i,\text{sim}} - n_{\text{gas}} \right), \quad (4)$$

where R_ϵ is a correction to the total efficiency in simulation.

Due to the slow variation of the differential cross-section in η , only six intervals in η are used with $\Delta\eta = 0.5$. The width of the last interval, $\eta \in [4.5, 4.8)$, is reduced to match the acceptance of the tracking system. Since the differential cross-section has a power-law shape in p_T , 50 logarithmic intervals are used in the range $p_T \in [0.01, 10.00)$ GeV/ c with $\Delta\log_{10}(p_T/(\text{GeV}/c)) = 0.06$. The limit of the kinematic acceptance, *i.e.* the minimum momentum of approximately 2 GeV/ c for a particle to reach the tracking stations downstream of the magnet, introduces a lower limit on p_T depending on η . In this analysis, a tighter requirement $p > 5$ GeV/ c is used, since a correction of the efficiency, which is described in Sect. 4, is based on the two control measurements presented in Refs. [26, 27], which both applied this requirement.

The track-reconstruction efficiency depends on the detector occupancy. To ensure that the simulation reproduces the occupancy observed in data, weights are assigned to the simulated events. The number of tracks that traverse the entire tracking system is used as a proxy for the occupancy. Simulated events are weighted by the ratio of the distributions of the number of these tracks in data and simulation according to the occupancy of the event. Each of the two simulated samples is weighted to reproduce the occupancy of the LHC fill with the same magnetic-field configuration. As a cross-check, the chosen proxy for the occupancy is compared to an alternative proxy, the number of hits in the scintillating-pad detector, which is not affected by possible artefacts of the track reconstruction. A linear relation is observed between the number of tracks that traverse the entire tracking system and the number of hits in the scintillating-pad detector, confirming this choice of the proxy for the detector occupancy.

The ROOT [28] and LHCb [29, 30] software frameworks are used for the initial data preparation, while the analysis is written in the PYTHON language with standard scientific packages [31–36] and high-energy-physics-specific packages [37–40] from the SCIKIT-HEP project [41].

4 Efficiencies

The total efficiency to observe prompt long-lived charged particles depends on the geometric acceptance of the detector, the track-reconstruction efficiency and the particle loss due to decays or interactions with the detector material. This loss depends on the particle composition and the amount of traversed material. The detector acceptance and the reconstruction efficiency are taken from simulation, and validated against data [26]. For the two other types of efficiencies, corrections are applied in each kinematic interval, which are described in the following.

First, the track-reconstruction efficiency is corrected. This is based on results of a separate control measurement [26], in which muon tracks from $J/\psi \rightarrow \mu^+\mu^-$ decays were studied to determine ratios of the track-reconstruction efficiencies in data and simulation in intervals of η and p . A linear transformation matrix is built to map the results of the efficiency ratios in the control measurement, which was performed in different kinematic

intervals, onto the intervals of this measurement. Non-uniform track density is accounted for in this transformation. The obtained efficiency ratios are identical for both particle charges and are used as the first component of the correction to the efficiency in simulation. The uncertainty of this component is between 1 % and 5 % over the kinematic range.

Second, the simulated particle composition is corrected by splitting the charged particles into four classes per charge; charged pions, charged kaons, protons, and a category for all other prompt long-lived charged particles; and then adjusting the relative yield of each class. As this composition has not yet been measured in pp collisions at $\sqrt{s} = 13$ TeV, measurements of ratios of prompt hadron production in pp collisions at $\sqrt{s} = 0.9$ TeV and 7 TeV that were performed by the LHCb collaboration [27] are extrapolated to 13 TeV. The extrapolations of the \bar{p}/p , $(K^+ + K^-)/(\pi^+ + \pi^-)$ and $(p + \bar{p})/(\pi^+ + \pi^-)$ ratios are defined as linear functions of $\ln \sqrt{s}$. The largest deviations of up to 40 % are observed between the extrapolated and simulated $(p + \bar{p})/(\pi^+ + \pi^-)$ ratios.

Then, double ratios of the extrapolated hadron ratios and the corresponding ratios of the particle counts in simulation are formed. For each η interval and each particle charge, corrections to the counts of charged pions, charged kaons, protons and other prompt long-lived charged particles in simulation are defined as functions linear in $\ln p_T$. To determine the corrected particle counts for the last three of these particle classes, double ratios of the hadron ratios obtained from the corrected particle counts and the hadron ratios obtained from the original particle counts in simulation are fitted to the double ratios from the extrapolations. The double ratios that are fitted have only a small variability within the η and p_T intervals of the control measurement, over which the particle counts are integrated, reflecting that no strong dependence on these variables is observed. The corrected count of charged pions is computed from the condition that the composition correction cannot change the total number of particles. The reference hadron ratios do not cover the intervals $\eta \in [2.0, 2.5)$ and $\eta \in [4.5, 4.8)$. In these intervals, the values from the corresponding adjacent η interval are used. As the corrected particle counts cannot completely be determined from the available data, Gaussian penalty terms are introduced as a regularisation to suppress deviations above 5 % of the corrected counts from their initial values.

For each charge, the composition-corrected efficiency in simulation is computed by summing the products of the efficiencies for the four particle classes and their corrected fractions. The efficiencies, ε_{sim} , are shown in Fig. 1. The efficiency for the fourth class of other prompt long-lived charged particles is the lowest, because this class contains Σ^+ , Σ^- , Ξ^- and Ω^- baryons and their antiparticles, which have the shortest lifetimes. The correction is not charge symmetric due to different hadronic-interaction cross-sections of each particle and its antiparticle, inducing different efficiencies. The systematic uncertainty of this correction dominates over its statistical uncertainty. Half of the correction is assigned as a systematic uncertainty as a conservative estimate, which is at most 2.5 %.

Material interactions contribute to the uncertainty of the corrected efficiency as the simulated amount of material has an uncertainty of 10 %, which is described in Ref. [26]. Here, the interaction losses of charged pions and charged kaons are estimated to be 14 % and 11 %, respectively. For protons, the loss can be estimated from the difference between the efficiency for protons in simulation and that for muons. Since protons do not decay, any loss relative to muons, for which interactions are negligible, is caused by material interactions. The loss is found to be between 20 % and 30 % across the full kinematic range. It is generally larger at low p_T and for antiprotons across the full kinematic range.

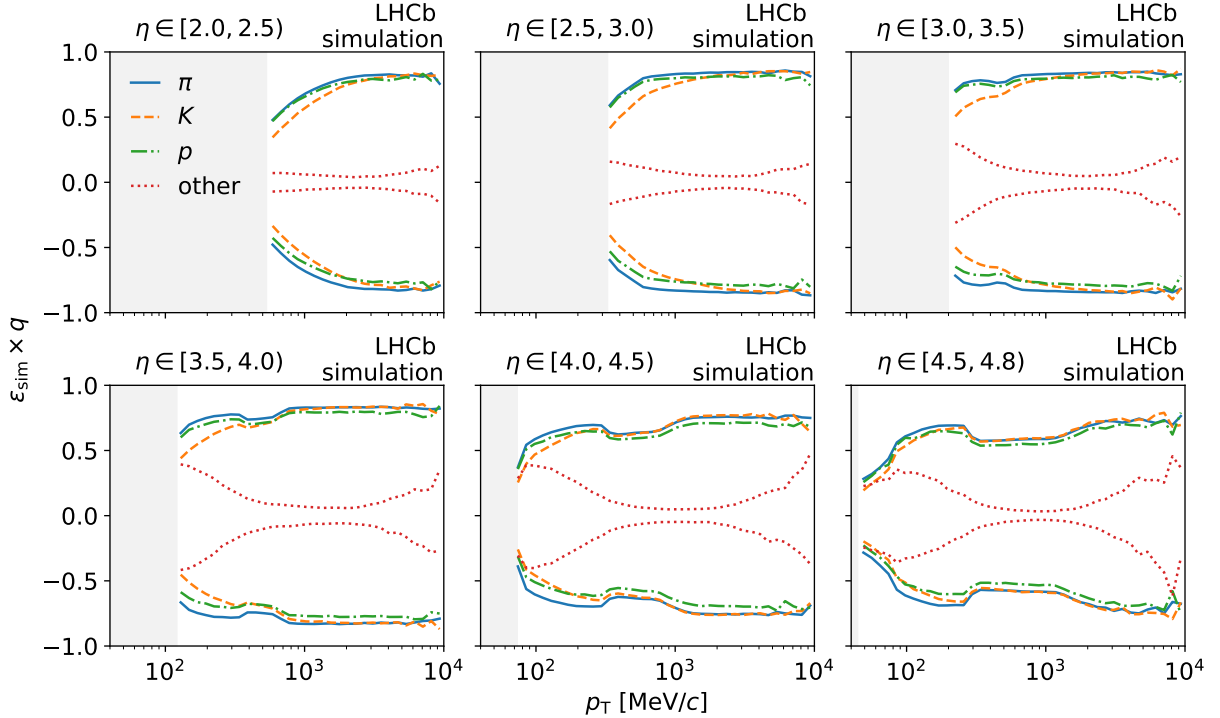


Figure 1: Efficiencies for different particle species in intervals of η and as a function of p_T for the simulated sample generated with the magnetic field pointing upwards. The product of the efficiency and the particle charge in units of the elementary charge is shown to separate values for oppositely charged particles. The light-grey areas indicate the limit of the kinematic acceptance.

These losses and their uncertainty are proportional to the amount of material. In the computation of the corresponding uncertainty of the efficiency, the uncertainties of the individual efficiencies for pions, kaons and protons contribute according to their corrected fractions. This results in an uncertainty of approximately 1%. The contribution from other prompt long-lived charged particles is neglected as their loss is dominated by decays and not by material interactions.

The combined correction is shown in Fig. 2 and reduces the original efficiency in simulation by up to 5% for negatively charged particles. This reduction arises primarily from the increase in the fraction of other prompt long-lived charged particles, which have a lower efficiency.

The systematic uncertainty of the corrected efficiency is the sum of the contributions from the ratios of track-reconstruction efficiencies, the particle-composition correction, material interactions and the statistical uncertainty of the simulated samples. This uncertainty ranges between 0.06% and 2%, depending on the kinematic interval, while the total uncertainty ranges from 0.9% to 5.1%.

5 Background contributions

The origins of the candidate tracks in simulation are shown in Fig. 3. Prompt long-lived charged particles constitute more than 85% of the candidate tracks around $p_T = 1$ GeV/c, but towards lower or higher values of p_T , the background contributions increase. These

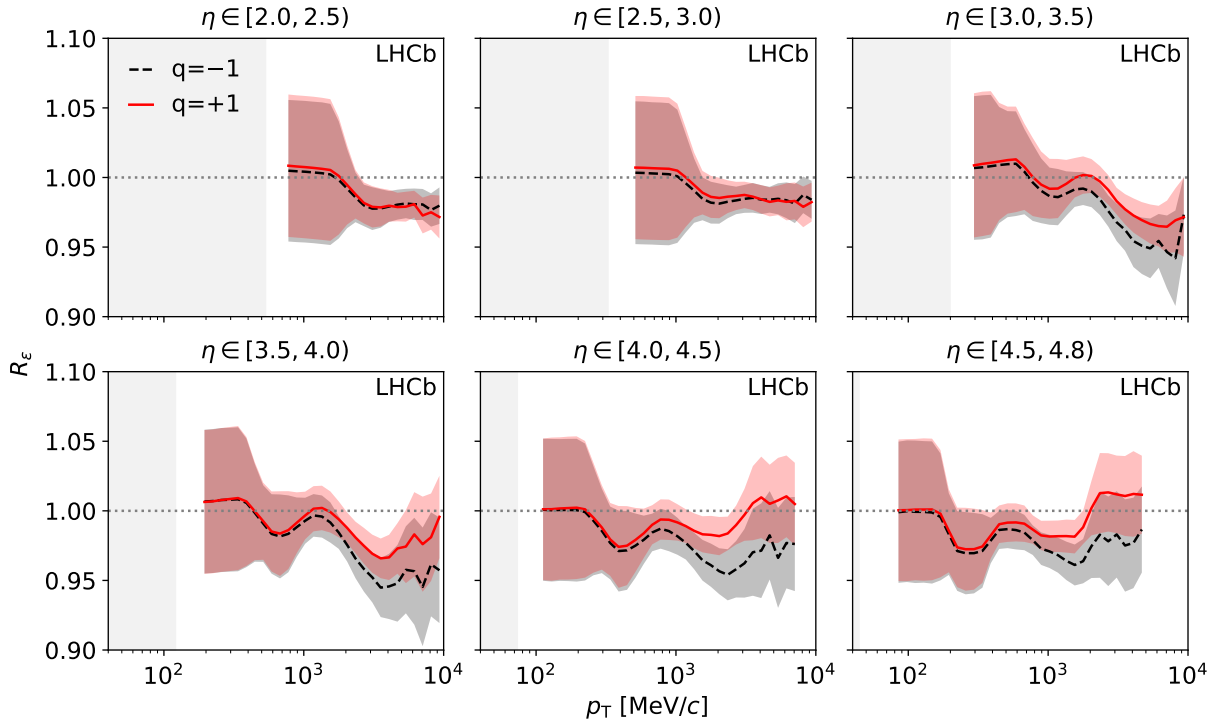


Figure 2: Efficiency corrections, R_ε , for positively and negatively charged particles in intervals of η and as a function of p_T for the simulated sample generated with the magnetic field pointing upwards. The bands indicate the systematic uncertainty. The light-grey areas represent the limit of the kinematic acceptance. The gap between this limit and the correction is due to the tighter requirement of $p > 5 \text{ GeV}/c$ applied to the control measurements on which this correction is based.

background contributions are quantified using simulation and adjusted with correction factors from proxies obtained from data and simulation. The background contributions that are sufficiently large to require a correction are: fake tracks, tracks originating from material interactions of charged pions and from photon conversions, and tracks produced in decays of strange hadrons. In the following subsections, the proxies constructed for these sources of background are presented. The remaining sources, which are not adjusted, are combined and an uncertainty of 50% is assumed for their contribution. The uncertainty of the differential cross-section resulting from this assumption is negligible, as the contribution from the remaining sources of background is small.

5.1 Fake tracks

The largest background at the limits of the analysed p_T range is from fake tracks. These are characterised by having a low quality of the track fit and missing hits in instrumented detector parts. This information is combined with further variables from the tracking system to estimate a fake-track probability, P_{fake} . The imposed selection requirement, $P_{\text{fake}} < 0.3$, rejects between 40% and 80% of the fake tracks and retains 99% of the real tracks.

For each kinematic interval and each particle charge, data and simulation are divided into ten equal-width intervals in the P_{fake} variable. Distributions in two different kinematic

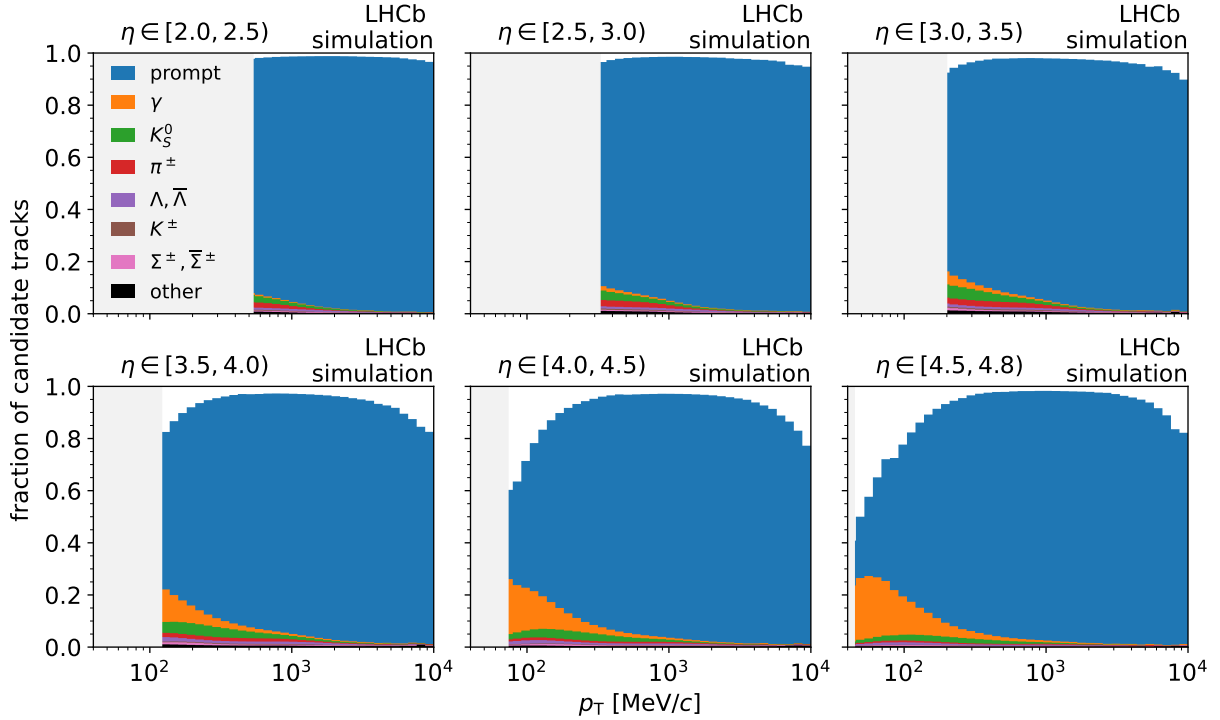


Figure 3: Origins of the candidate tracks in intervals of η and as a function of p_T for the simulated sample generated with the magnetic field pointing upwards. The *prompt* category refers to the signal tracks, while the other categories correspond to non-prompt tracks originating from the listed parent particles and include both decays and material interactions. Fake tracks are indicated by the white areas above the stacked histograms. The light-grey areas represent the limit of the kinematic acceptance.

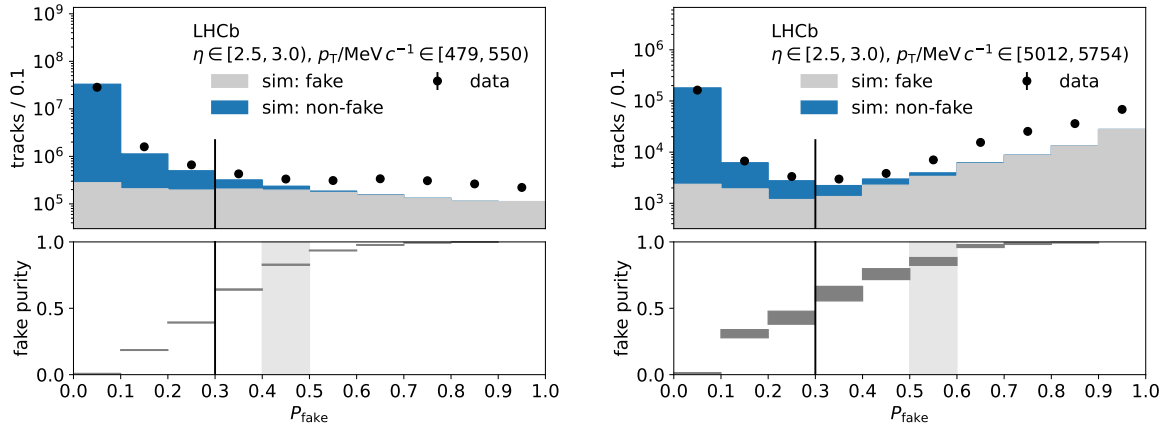


Figure 4: Distributions of P_{fake} in a kinematic interval (left) at low p_T and (right) at high p_T for the LHC fill recorded with the magnetic field pointing upwards and the simulated sample with the same magnetic-field configuration. The statistical uncertainty of the data is indicated by error bars, but they are not visible on these scales. The purity of the proxy is shown in the lower subplots, where light-grey boxes represent the P_{fake} interval selected to determine the proxy. Vertical lines indicate the threshold $P_{\text{fake}} < 0.3$ for candidate tracks.

intervals are given as examples in Fig. 4. In simulation, a pure sample of fake tracks is present at high P_{fake} values. Generally, good agreement is found in the shapes of the P_{fake} distributions between data and simulation, but in simulation, fewer fake tracks are observed. Consequently, a correction is used to adjust the simulated contribution from fake tracks.

The number of tracks in the first interval of the P_{fake} distribution above 0.3, where the fake-track purity is greater than 80%, is chosen as a proxy for fake tracks. This choice balances two sources of systematic uncertainty. A P_{fake} interval with a high fake-track purity is required in order to select a proxy that is insensitive to possible differences in the number of signal tracks between data and simulation, which would favour the interval with the highest purity. However, selecting an interval close to the P_{fake} region of interest, $P_{\text{fake}} < 0.3$, minimises the impact of shape differences in the P_{fake} distributions between data and simulation.

The uncertainty of the fake-track proxy is the quadratic sum of statistical and systematic contributions. The statistical uncertainty is propagated from the track counts in data and simulation. The systematic uncertainty is estimated by computing an alternative proxy. For this, the integral of the track counts in the selected P_{fake} interval and all the intervals above is used. The alternative proxy is more affected by shape differences and is therefore an upper limit on the systematic error. This type of systematic variation is modelled with a uniform distribution of deviations of which the upper limit corresponds to the alternative proxy, while the centre is the value of the default proxy. The uncertainty of the proxy is then given by the standard deviation of this distribution.

The mean of the resulting proxy ratios between the two particle charges is shown in Fig. 5. At low η , values of the proxy ratio of up to 2.8 are observed, but in those kinematic intervals in which the background from fake tracks is large, the ratio is between 1.2 and 1.4. In general, the ratio is smooth as a function of p_{T} . Discontinuities in the range $\eta \in [2.5, 3.5)$ are caused by changes of the P_{fake} interval chosen to determine the proxy.

5.2 Material interactions

Non-prompt tracks produced in material interactions constitute the second-largest source of background. As only tracks that traverse the entire tracking system are used, these are interactions occurring inside the vertex detector. Electrons originating from photon conversions, which populate mainly the kinematic intervals at high η and low p_{T} , contribute up to 20% to the candidate tracks, while charged particles stemming from hadronic material interactions of charged pions contribute less than 5%.

The number of tracks originating from charged-pion material interactions is proportional to the product of the total particle flux, consisting primarily of charged pions, and the amount of traversed material. The number of tracks included in vertices comprising three tracks is chosen as a proxy for this product. The threshold of three tracks is used because hadronic interactions frequently produce three or more charged particles, while decays into three or more charged particles are rare in the analysed data sample. This approach is similar to that presented in Ref. [42]. Instead of defining a separate proxy for photon conversions, their simulated yield is scaled with the proxy for charged-pion material interactions. This is motivated by the observation that most photons originate from decays of neutral pions, which are produced in a fixed ratio to charged pions due to

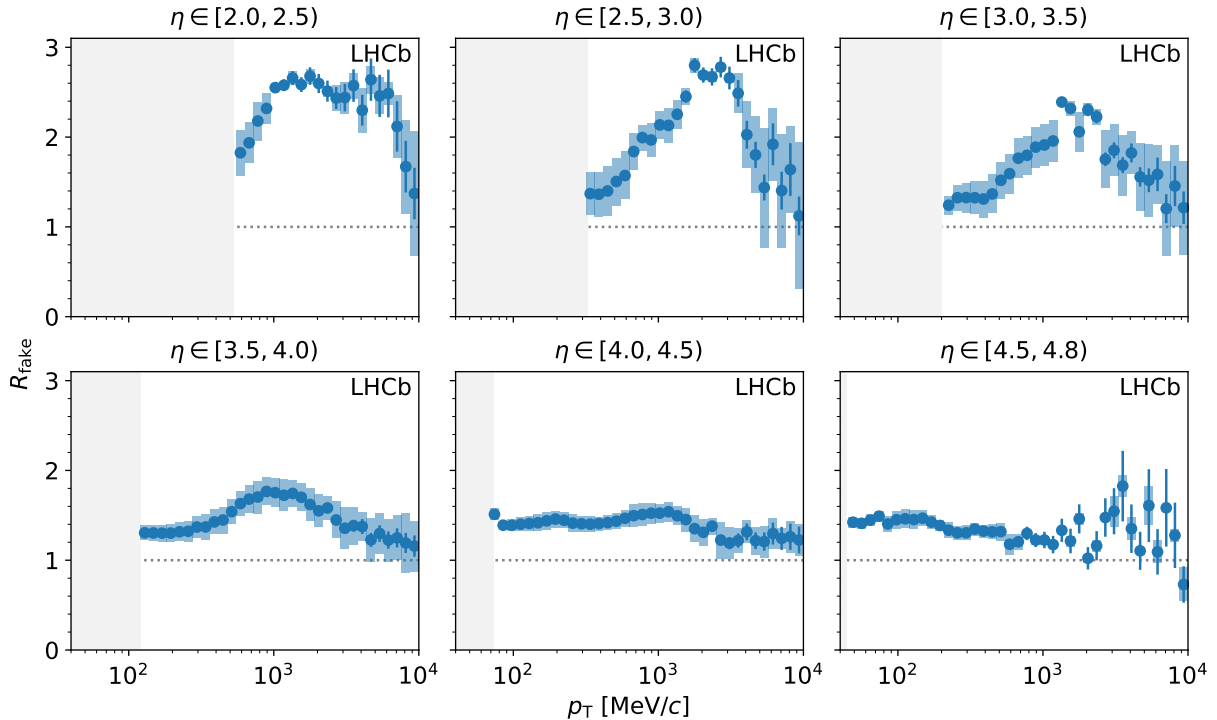


Figure 5: Ratio of the proxies for fake tracks in data and simulation in intervals of η and as a function of p_T for the LHC fill recorded with the magnetic field pointing upwards and the simulated sample with the same magnetic-field configuration. The mean of the proxy ratios for positively and negatively charged particles is shown. The error bars indicate the statistical uncertainty, and the boxes indicate the systematic uncertainty. The light-grey areas represent the limit of the kinematic acceptance.

isospin symmetry. Furthermore, the conversion probability of photons and the interaction probability of charged pions are both proportional to the amount of material.

In each event, all unique combinations of three candidate tracks are formed. Their point of closest approach is computed with a vertex fit minimising the sum of the squared distances of the tracks. This point is the candidate vertex of an interaction. To reduce combinatorial background, where three tracks are randomly associated with a common vertex, a lower limit is imposed on the distance of the vertex from the z axis, which points from the radial centre of the vertex detector along the beam axis towards the muon system and has its origin close to the average primary vertex. This discards the region in which no material is present.

The purity of the obtained sample of vertices is further increased by applying requirements that are optimised using simulation. First, a simultaneous optimisation of a lower limit on the z coordinate of the vertex and an upper limit on the sum of the squared distances of the tracks to their associated vertex, d , is performed without subdividing the sample in η and p_T . The z requirement suppresses combinatorial background by selecting vertices downstream of the region in which most of the primary vertices are reconstructed. The upper limit on d rejects random combinations by requiring that the tracks are compatible with originating from a single point. Second, an optimisation of a lower limit on the mass of the three-track combination is performed separately for each kinematic interval. As the species of the produced particles are not known, a zero-mass

hypothesis is assigned to each track. Wider p_T intervals are used in this study to reduce fluctuations in the proxy ratio to be determined, created by successively merging groups of three adjacent p_T intervals. The mass requirement further suppresses the combinatorial background. For both optimisations, the figure of merit $S/\sqrt{S+B}$ is used, where S denotes the number of tracks that represent the signal for this proxy, and B is the number of background tracks. The requirements chosen are those that maximise the value of the figure of merit. This results in a lower limit on z of 290 mm and an upper limit on d of 0.1 mm^2 .

After the application of all optimised requirements, the contribution from charged pions is approximately equal in size to that from other particles, *e.g.* kaons or protons. For each kinematic interval and each particle charge, the number of tracks that are included in selected vertices is used as the proxy. In the first two η intervals and around $p_T = 0.5 \text{ GeV}/c$, the highest values of the purity of charged-pion interactions are obtained, which range from 40 % to 45 %. Towards higher values of η and lower or higher values of p_T , the purity decreases.

The proxy ratio is independent of the purity for kinematic intervals with purities above 30 %. Therefore, the value of the proxy ratio, R_{mat} , is only used if the purity in the kinematic interval under consideration is greater than the threshold value of 30 %. Moreover, an upper limit of 30 % is imposed on the statistical uncertainty of the purity to reject intervals that contain only a small number of tracks. As a substitute for the values of the proxy ratio in the intervals below the purity threshold, the median of the values of the proxy ratio in the intervals above the threshold is computed. The uncertainty of this median value is estimated assuming a uniform distribution covering the observed range of R_{mat} .

The systematic uncertainty of the proxy for material interactions is determined by loosening and tightening the optimised z and d requirements and computing alternative proxy ratios, R'_{mat} . The mass requirement is not varied, as a good agreement is found in the shapes of the distributions between data and simulation in all kinematic intervals. Deviations in some of the alternative proxies cannot be explained by statistical fluctuations and are therefore considered as a systematic uncertainty. The deviation of an alternative is considered significant if the condition

$$(R'_{\text{mat}} - R_{\text{mat}})^2 > |\sigma^2(R'_{\text{mat}}) - \sigma^2(R_{\text{mat}})| \quad (5)$$

is fulfilled, where σ^2 denotes the variance, which is a consequence of using the same data set to determine the default proxy ratio and the alternatives. Following Ref. [43], the systematic uncertainty is taken as the standard deviation of the variations that differ significantly and the initial ratio is replaced with the mean of the significant variations. This procedure is applied to the values of the proxy ratio in the kinematic intervals above the purity threshold and to the median value computed for the other intervals. The values and the resulting uncertainties of the proxy ratio are shown in Fig. 6.

5.3 Strange-hadron decays

Up to 7 % of the candidate tracks are non-prompt tracks produced in decays of strange hadrons inside the vertex detector. Approximately 80 % of these tracks originate from $K_S^0 \rightarrow \pi^+\pi^-$, $\Lambda \rightarrow p\pi^-$ and $\bar{\Lambda} \rightarrow \bar{p}\pi^+$ decays. The number of K_S^0 mesons and Λ and $\bar{\Lambda}$

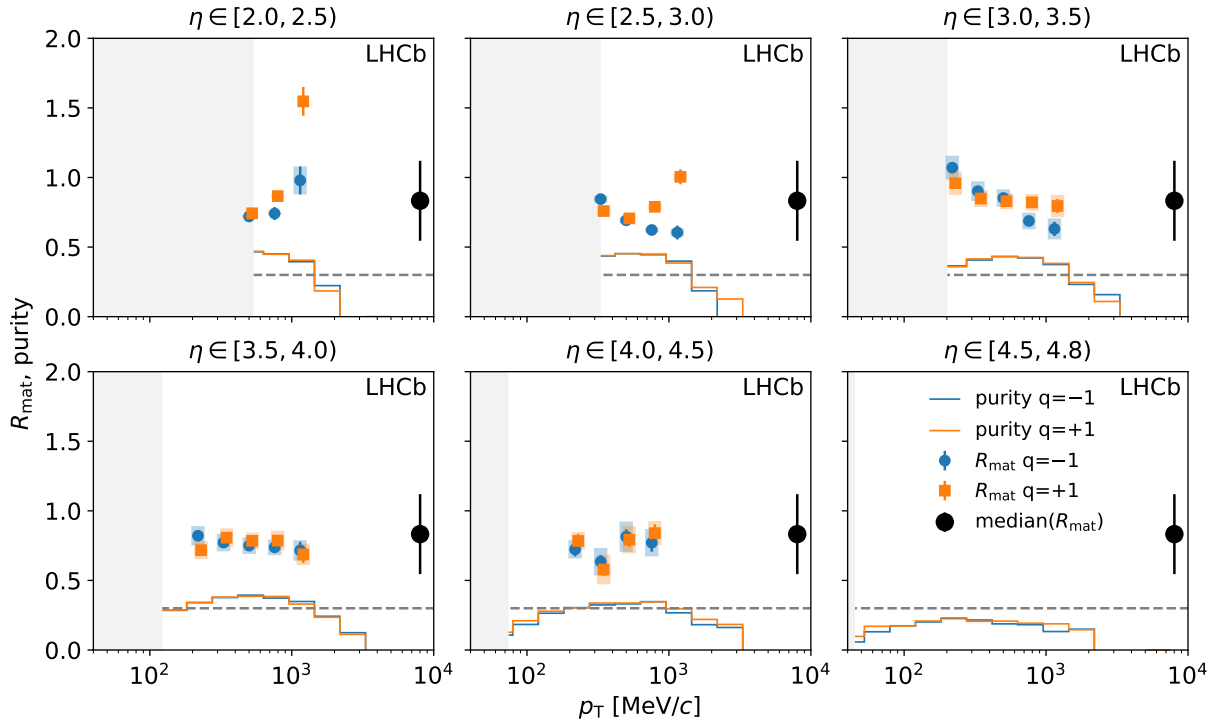


Figure 6: Ratio of the proxies for material interactions in data and simulation and purity of the proxy in intervals of η and as a function of p_T for the LHC fill recorded with the magnetic field pointing upwards and the simulated sample with the same magnetic-field configuration. The quantities are shown separately for positively and negatively charged particles. The error bars indicate the statistical uncertainty, and the boxes indicate the systematic uncertainty. The points are slightly displaced horizontally within the p_T intervals to increase the visibility. The dashed grey lines represent the purity threshold. The larger points indicate the median value computed for the intervals below the threshold. The light-grey areas represent the limit of the kinematic acceptance.

baryons, of which both decay products create a candidate track, is chosen as a proxy for this background.

Candidate decays are obtained by forming pairs of oppositely charged candidate tracks. A small set of loose requirements is used to maintain high selection efficiency for strange decays. The distance of closest approach of the two tracks is required to be less than 1 mm and the distance along the z axis of their point of closest approach from the average primary vertex is required to be greater than 150 mm. For K_S^0 candidates, the mass is computed by assigning the pion-mass hypothesis to both tracks, while for Λ and $\bar{\Lambda}$ candidates, the proton- and pion-mass hypotheses are assigned to the tracks.

The distributions of K_S^0 and Λ candidates in one kinematic interval are shown as examples in Fig. 7. Extended-maximum-likelihood fits [44] to the mass distributions of the K_S^0 , Λ and $\bar{\Lambda}$ candidates in data and simulation are performed separately for each (η, p_T) interval of their kinematic distributions. As in case of the proxy for material interactions, wider p_T intervals are used in this study, obtained by merging groups of three adjacent p_T intervals. In the fits, the K_S^0 , Λ or $\bar{\Lambda}$ signal is modelled with a nonstandardised Student's t-distribution with free location and width parameters. The background, which is only combinatorial, is modelled with a third-degree Bernstein polynomial. The yields

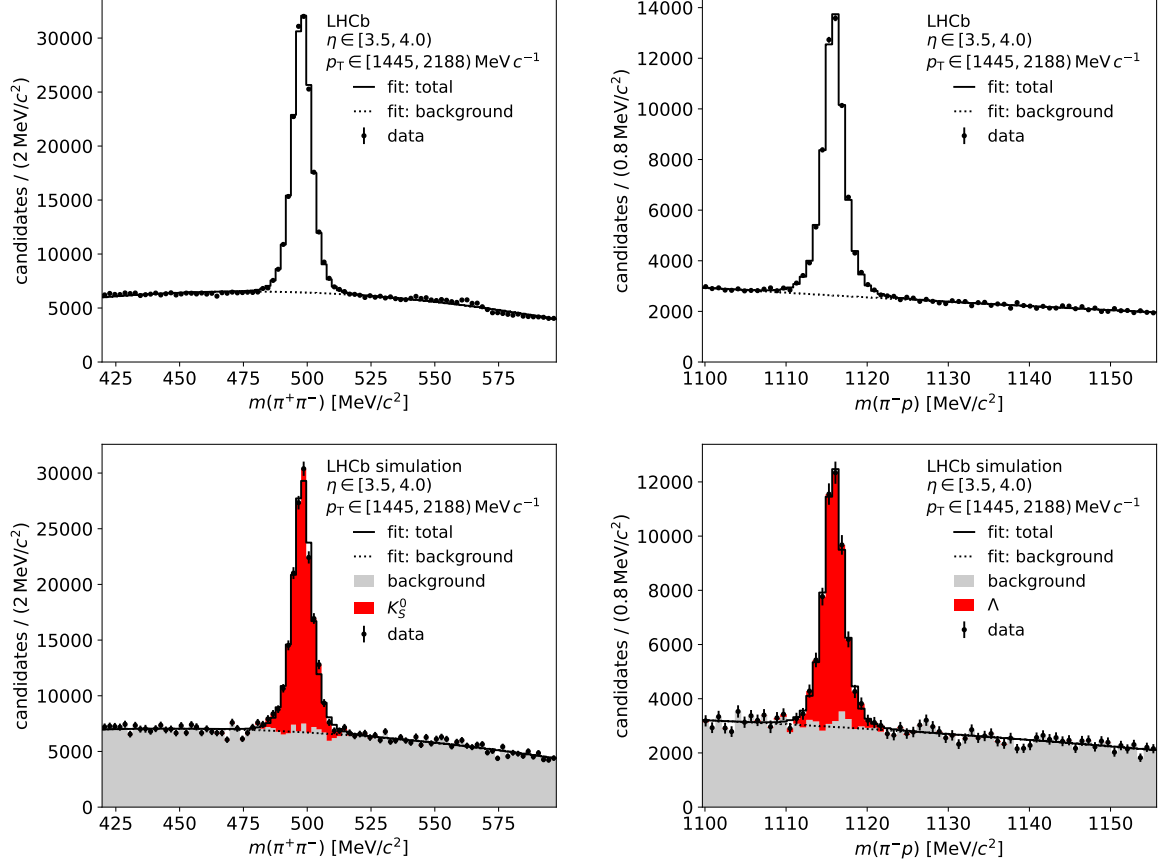


Figure 7: Mass distributions of (left) K_S^0 and (right) Λ candidates in one kinematic interval for (top) the LHC fill recorded with the magnetic field pointing upwards and (bottom) the simulated sample with the same magnetic-field configuration. Solid lines indicate the total fit and dotted lines the background. In the case of simulation, the signal and background contributions are shown for illustration, but this information is not used in the analysis.

in each interval of the mass distributions are modelled with Poisson distributions for the unweighted histograms in data and with scaled Poisson distributions [45] for the occupancy-weighted histograms in simulation.

The ratios of the signal yields in data and simulation are only computed in those kinematic intervals where a signal peak is present with a significance of at least three standard deviations. The ratios of the signal yields are shown in Fig. 8. In all η intervals and for all three strange-hadron species, a pattern is observed in the yield ratios as a function of p_T . This is interpreted as a general difference in the amount of produced strange quarks between data and simulation, since it is the same for a meson and a baryon. The pattern is modelled with a monotone cubic spline [46]. A least-squares fit of the model to the yield ratios is performed, in which a Gaussian penalty term is added in order to restrict the value of the spline at the upper limit of the p_T range, where no data points are present.

The fitted model is then used to determine the proxy ratio of the strange hadrons, R_{parent} , over the full kinematic range. However, the background for prompt long-lived charged particles is caused by the decay products of these hadrons. The proxy ratio of the

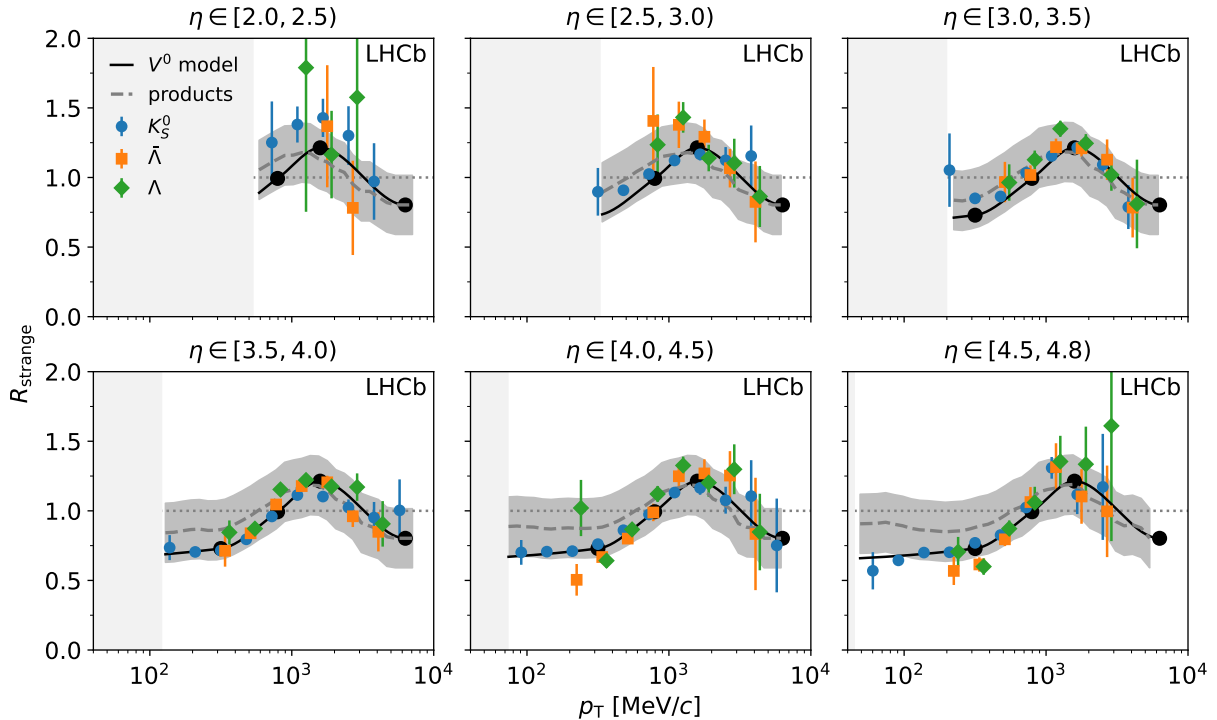


Figure 8: Ratio of the proxies for strange-hadron decays in data and simulation in intervals of η and as a function of p_T for the LHCb recorded with the magnetic field pointing upwards and the simulated sample with the same magnetic-field configuration. The V^0 model lines indicate the interpolated K_S^0 , Λ and $\bar{\Lambda}$ yield ratios, with support points indicated by black dots. The lines labelled as *products* represent the proxy ratio of the decay products, with the bands representing the propagated systematic uncertainty. The light-grey areas indicate the limit of the kinematic acceptance.

products, R_{strange} , in the (η, p_T) intervals of their kinematic distributions is computed as

$$R_{\text{strange}, kl} = \frac{\sum_{h, ij} n_{h, ijkl} R_{\text{parent}, j}}{\sum_{h, ij} n_{h, ijkl}}, \quad (6)$$

where: h is $K_S^0, \Lambda, \bar{\Lambda}$; i and j iterate through the η and p_T intervals of the kinematic distributions of the parent particles, respectively; k and ℓ iterate through the η and p_T intervals of the kinematic distributions of the decay products, respectively; and n is the simulated yield of the decay products in the corresponding intervals. The ratio R_{strange} is closer to unity than the ratio R_{parent} , as the broad kinematic distributions of the decay products dilute deviations. The statistical uncertainty of the fitted model is negligible compared to the systematic uncertainty suggested by the deviations of the yield ratios from the model. A systematic uncertainty of $\pm 15\%$ is assigned to the proxy ratio to cover these deviations.

6 Results

The differential cross-section of prompt inclusive production of long-lived charged particles is determined with Eqs. (1) and (4). The fraction of candidate tracks originating from

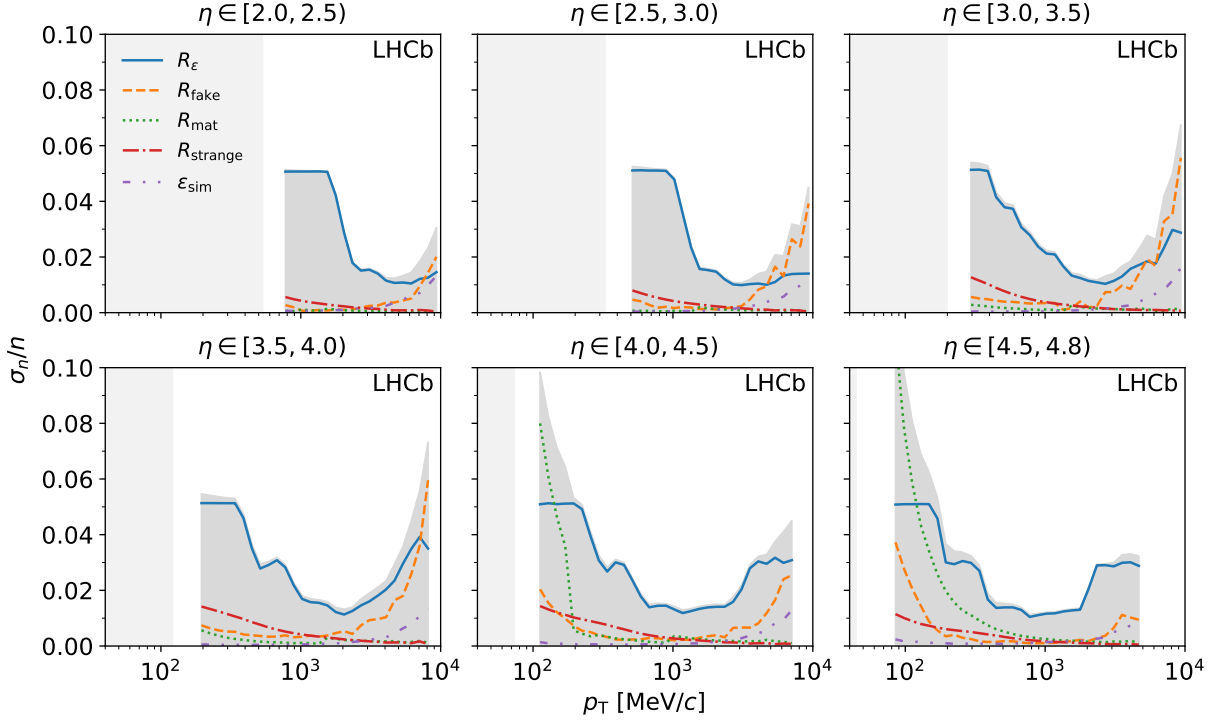


Figure 9: Leading sources of relative uncertainties of the number of prompt long-lived charged particles in intervals of η and as a function of p_T for the LHC fill recorded with the magnetic field pointing upwards. The total uncertainty, represented by the grey envelopes, excludes the uncertainty of the integrated luminosity of 2.0%. The light-grey areas indicate the limit of the kinematic acceptance.

beam-gas interactions is found to be 1% for the LHC fill recorded with the magnetic field pointing downwards, independent of the kinematic interval. For the fill recorded with the magnetic field pointing upwards, the fraction is below the level of 0.1%.

The detector resolution distorts the measured kinematic distributions, by inducing migration between different (η, p_T) intervals. This distortion is between 1% and 2%, depending on the kinematic interval. The total efficiency, ϵ , in this analysis implicitly takes these migration effects into account. It is calculated from simulation as the ratio of the number of candidate tracks that can be associated with signal particles and the respective number of signal particles, where the candidates are sorted into intervals using the reconstructed momenta, while the signal particles are sorted into intervals using the generated momenta. Deviations between the shapes of the kinematic distributions of charged particles in data and simulation can introduce a bias in this approach, but the bias in this case is estimated to be at the order of 0.01% and therefore negligible.

The statistical uncertainty of the data sample is subdominant in the full kinematic range, reaching 1.5% at high p_T . Non-Poissonian statistical fluctuations of the candidate counts in kinematic intervals are taken into account. Each event contributes entries to a number of kinematic intervals, introducing statistical correlations of up to 0.4 between intervals, and variances that are up to 50% larger than the Poisson expectation. The covariance matrix of these statistical fluctuations is estimated by dividing the full sample into 100 equivalent subsets, computing the covariance of the subsets and extrapolating the result back to the full data set.

Table 1: Statistical and systematic uncertainties affecting the measured differential cross-section.

Source	Relative uncertainty in %
Statistical uncertainty of the data sample	0.0–1.5
Total efficiency	0.9–5.1
Beam-gas interactions	0.0–1.7
Fake tracks	0.1–9.5
Material interactions	0.0–12
Strange-hadron decays	0.0–1.5
Other background contributions	0.1–1.1
Integrated luminosity	2.0
Total uncertainty	2.3–15

The uncertainty on the differential cross-section is computed from the uncertainties of the individual terms in Eqs. (1) and (4) using full error propagation of the respective covariance matrices. The contributions to the uncertainty of the number of prompt long-lived charged particles are shown in Fig. 9. The correction of the track-reconstruction efficiency is the largest contribution in most intervals. In the range $\eta \in [2.0, 4.0)$ and at high p_T , the uncertainty of the proxy for fake tracks dominates, while in the range $\eta \in [4.0, 4.8)$ and at low p_T , the uncertainty of the proxy for material interactions contributes most.

The final results are obtained by computing the average of the differential cross-sections separately calculated for each LHC fill, after confirming that the two separate results are consistent with each other. As a further cross-check, data from six other fills, recorded at the same centre-of-mass energy and with the same trigger as the default data sample, are compared and found to be consistent with the main result.

The calculation of the covariance matrix of the combined result takes into account that the fills have correlated and uncorrelated uncertainties. Uncorrelated are the statistical uncertainties and the systematic uncertainties of the proxy for fake tracks and of the proxy for material interactions in the kinematic intervals above the purity threshold. Correlated uncertainties are all other systematic uncertainties and the uncertainty of the integrated luminosity. The covariance matrix of the final result is computed assuming that the uncertainties that are fully correlated within a fill are also fully correlated between the two fills.

The minimum and maximum values over all kinematic intervals for the uncertainties from each source that contribute to the final result are listed in Table 1. The total uncertainty of the differential cross-section is between 2.3% and 15%, which includes the fully correlated systematic uncertainty of 2.0% from the integrated luminosity. The correlations are nonzero and positive between kinematic intervals and the two particle charges, since the systematic uncertainties dominate. The correlation matrix of the final differential cross-section is shown in Appendix B.

The measured differential cross-section of prompt inclusive production of long-lived charged particles is shown in Fig. 10. The values for positively and negatively charged particles are listed in Appendix A. In the figure, the measurement is compared with the predictions from the hadronic-interaction models PYTHIA 8.3 [18] with the default Monash tune [50], EPOS-LHC [14], QGSJET II-04 [15] and SIBYLL 2.3d [11]. The latter three

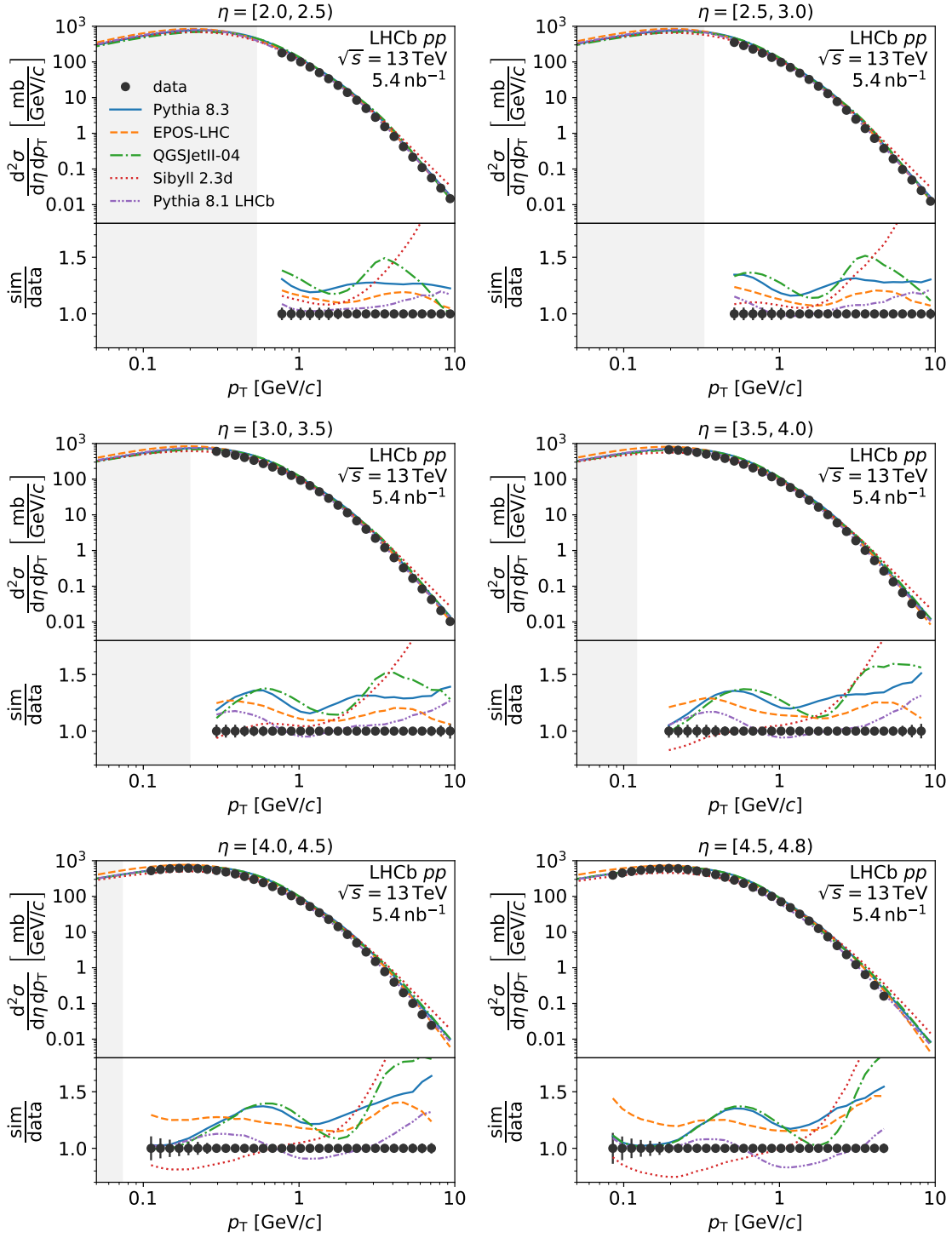


Figure 10: Differential cross-section of inclusive production of prompt long-lived charged particles in intervals of pseudorapidity, η , and as a function of transverse momentum, p_T . The error bars indicate the total uncertainty. The ratios of the model predictions and this measurement are shown in the lower subplots. The lines labelled as *Pythia 8.1 LHCb* correspond to the weighted simulated samples of this analysis.

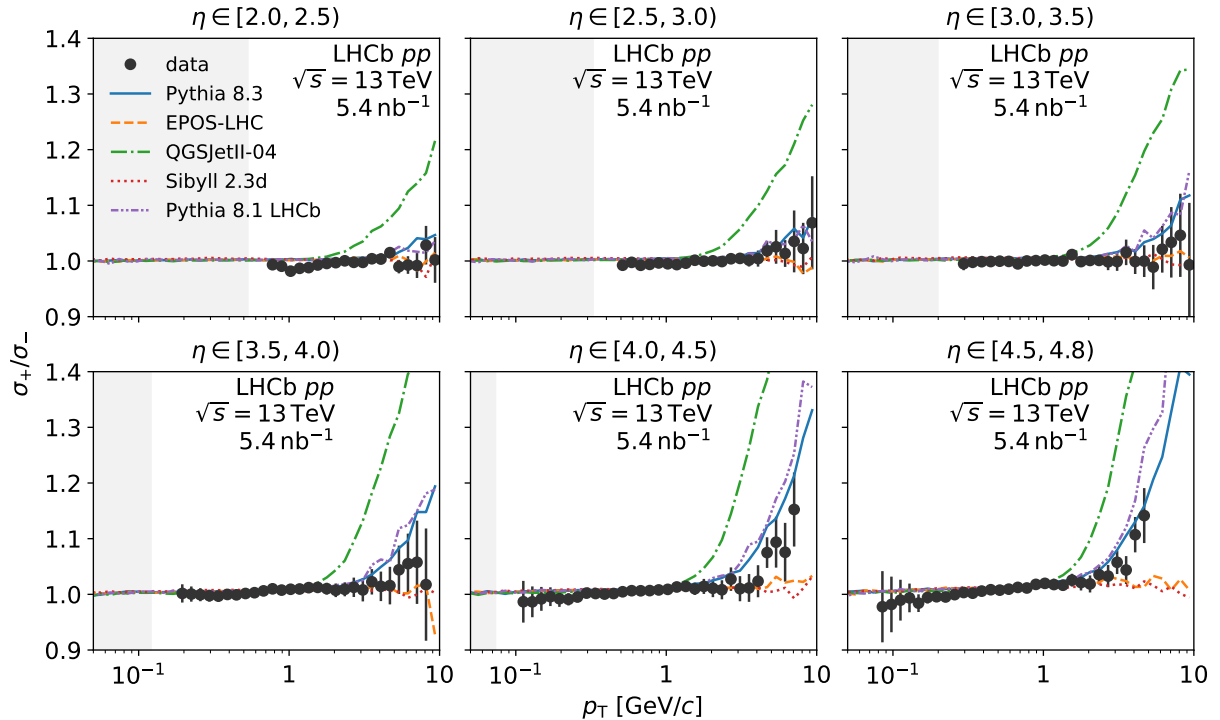


Figure 11: Ratios of the differential cross-sections of inclusive production of prompt long-lived positively and negatively charged particles as a function of transverse momentum and pseudorapidity for the data and the models shown in Fig. 10.

Table 2: Inelastic cross-sections used in the models of which the predictions are compared with this measurement and values from recent measurements at the LHC.

Model or experiment	Inelastic cross-section in mb
PYTHIA 8.3 [18]	78.05
EPOS-LHC [14]	78.98
QGSJET II-04 [15]	80.17
SIBYLL 2.3d [11]	79.86
ATLAS [47]	78.1 ± 2.9
LHCb [48]	75.4 ± 5.4
TOTEM [49]	79.5 ± 1.8

models are accessed through the CRMC package [51]. Also shown, but not comparable to the other models, is the occupancy-weighted LHCb tune of PYTHIA 8.1 that was used as the simulated sample in this analysis. The comparably good agreement of this simulation is based on the occupancy weighting, which removes deviations in the magnitude and leaves only deviations in the shape, while for the remaining models, deviations in the magnitude can occur. The calculation of the differential cross-section,

$$\frac{d^2\sigma}{d\eta dp_T} \equiv \frac{\sigma_{\text{inel}}}{N_{\text{inel}}} \frac{n}{\Delta\eta \Delta p_T}, \quad (7)$$

is based on: the inelastic cross-section, σ_{inel} , that is implemented in each model; the

number of generated inelastic events, N_{inel} ; and the number of prompt long-lived charged particles, n , in each kinematic interval. The inelastic cross-sections of the models and recent measurements are listed in Table 2.

The deviations of the predictions from the measured values are between -26% and $+170\%$. The models mostly overestimate the differential cross-section. These deviations are caused by differences in the kinematic distributions compared to the data as the implemented values of the inelastic cross-section are compatible with the performed measurements. The occupancy-weighted LHCb tune of PYTHIA 8.1, which is the weighted simulated sample used in this analysis, shows deviations between -17% and $+32\%$.

The ratio of the differential cross-sections for positively and negatively charged particles is shown in Fig. 11. The positively correlated components of the uncertainties cancel in the computation of the ratio. At high η and high p_{T} , the production of positively charged particles increases as the initial state has a charge of $+2$, which transfers to the final state in the forward region. This effect is predicted by the models to a varying extent. The best description of the ratio is provided by PYTHIA 8.3.

7 Summary

An unbiased measurement of the differential cross-section of prompt inclusive production of long-lived charged particles in pp collisions at $\sqrt{s} = 13$ TeV is presented. The data sample was recorded by the LHCb experiment and corresponds to an integrated luminosity of 5.4 nb^{-1} . The differential cross-section is measured as a function of transverse momentum and pseudorapidity in the ranges $p_{\text{T}} \in [0.08, 10.00) \text{ GeV}/c$ and $\eta \in [2.0, 4.8)$ and is determined separately for positively and negatively charged particles. An uncertainty between 2.3% and 15% is achieved. A comparison of the measured charge-combined differential cross-section with predictions from recent hadronic-interaction models shows that these models mostly overestimate the differential cross-section. The overall smallest deviations are observed for EPOS-LHC, while the ratio of the differential cross-sections for positively and negatively charged particles are best predicted by PYTHIA 8.3. The precision achieved in this measurement is essential for an improved simulation of the underlying event in collisions at the LHC and of interactions in the atmosphere of the Earth that cause air showers.

Acknowledgements

We express our gratitude to our colleagues in the CERN accelerator departments for the excellent performance of the LHC. We thank the technical and administrative staff at the LHCb institutes. We acknowledge support from CERN and from the national agencies: CAPES, CNPq, FAPERJ and FINEP (Brazil); MOST and NSFC (China); CNRS/IN2P3 (France); BMBF, DFG and MPG (Germany); INFN (Italy); NWO (Netherlands); MNiSW and NCN (Poland); MEN/IFA (Romania); MSHE (Russia); MICINN (Spain); SNSF and SER (Switzerland); NASU (Ukraine); STFC (United Kingdom); DOE NP and NSF (USA). We acknowledge the computing resources that are provided by CERN, IN2P3 (France), KIT and DESY (Germany), INFN (Italy), SURF (Netherlands), PIC (Spain), GridPP (United Kingdom), RRCKI and Yandex LLC (Russia), CSCS (Switzerland), IFIN-HH (Romania), CBPF (Brazil), PL-GRID (Poland) and NERSC (USA). We are

indebted to the communities behind the multiple open-source software packages on which we depend. Individual groups or members have received support from ARC and ARDC (Australia); AvH Foundation (Germany); EPLANET, Marie Skłodowska-Curie Actions and ERC (European Union); A*MIDEX, ANR, IPhU and Labex P2IO, and Région Auvergne-Rhône-Alpes (France); Key Research Program of Frontier Sciences of CAS, CAS PIFI, CAS CCEPP, Fundamental Research Funds for the Central Universities, and Sci. & Tech. Program of Guangzhou (China); RFBR, RSF and Yandex LLC (Russia); GVA, XuntaGal and GENCAT (Spain); the Leverhulme Trust, the Royal Society and UKRI (United Kingdom).

Appendices

A Differential cross-sections

The measured values of the differential cross-sections of prompt inclusive production of long-lived positively and negatively charged particles are listed in Table 3. The numerical values and the correlation matrix are provided in machine-readable form at [link].

Table 3: Differential cross-sections of prompt inclusive production of long-lived positively and negatively charged particles as a function of transverse momentum and pseudorapidity.

η	$\log_{10}(p_T/(\text{GeV}/c))$	$(d^2\sigma/(d\eta dp_T))/(\text{mb}/(\text{GeV}/c))$	
		$q = -1$	$q = +1$
[2.0, 2.5)	[-0.14, -0.08)	90 ± 5	89 ± 5
[2.0, 2.5)	[-0.08, -0.02)	68 ± 4	68 ± 4
[2.0, 2.5)	[-0.02, 0.04)	50.6 ± 2.8	49.7 ± 2.7
[2.0, 2.5)	[0.04, 0.10)	36.2 ± 2.0	35.7 ± 2.0
[2.0, 2.5)	[0.10, 0.16)	25.2 ± 1.4	24.9 ± 1.4
[2.0, 2.5)	[0.16, 0.22)	16.9 ± 0.9	16.8 ± 0.9
[2.0, 2.5)	[0.22, 0.28)	11.0 ± 0.5	11.0 ± 0.5
[2.0, 2.5)	[0.28, 0.34)	6.96 ± 0.24	6.94 ± 0.24
[2.0, 2.5)	[0.34, 0.40)	4.23 ± 0.12	4.23 ± 0.11
[2.0, 2.5)	[0.40, 0.46)	2.49 ± 0.06	2.48 ± 0.06
[2.0, 2.5)	[0.46, 0.52)	1.40 ± 0.04	1.40 ± 0.04
[2.0, 2.5)	[0.52, 0.58)	0.763 ± 0.019	0.766 ± 0.019
[2.0, 2.5)	[0.58, 0.64)	0.405 ± 0.010	0.406 ± 0.010
[2.0, 2.5)	[0.64, 0.70)	0.209 ± 0.005	0.212 ± 0.005
[2.0, 2.5)	[0.70, 0.76)	0.1079 ± 0.0026	0.1069 ± 0.0026
[2.0, 2.5)	[0.76, 0.82)	0.0550 ± 0.0014	0.0546 ± 0.0014
[2.0, 2.5)	[0.82, 0.88)	$(28.2 \pm 0.8) \cdot 10^{-3}$	$(28.0 \pm 0.8) \cdot 10^{-3}$
[2.0, 2.5)	[0.88, 0.94)	$(14.3 \pm 0.5) \cdot 10^{-3}$	$(14.7 \pm 0.5) \cdot 10^{-3}$
[2.0, 2.5)	[0.94, 1.00)	$(7.37 \pm 0.28) \cdot 10^{-3}$	$(7.39 \pm 0.28) \cdot 10^{-3}$
[2.5, 3.0)	[-0.32, -0.26)	177 ± 10	175 ± 10
[2.5, 3.0)	[-0.26, -0.20)	144 ± 8	144 ± 8
[2.5, 3.0)	[-0.20, -0.14)	115 ± 6	114 ± 6

η	$\log_{10}(p_T/(\text{GeV}/c))$	$(d^2\sigma/(d\eta dp_T))/(\text{mb}/(\text{GeV}/c))$	
		$q = -1$	$q = +1$
[2.5, 3.0)	[-0.14, -0.08)	89 ± 5	88 ± 5
[2.5, 3.0)	[-0.08, -0.02)	67 ± 4	67 ± 4
[2.5, 3.0)	[-0.02, 0.04)	49.1 ± 2.6	48.8 ± 2.6
[2.5, 3.0)	[0.04, 0.10)	35.1 ± 1.4	34.9 ± 1.4
[2.5, 3.0)	[0.10, 0.16)	24.3 ± 0.8	24.2 ± 0.8
[2.5, 3.0)	[0.16, 0.22)	16.2 ± 0.4	16.2 ± 0.4
[2.5, 3.0)	[0.22, 0.28)	10.40 ± 0.27	10.39 ± 0.27
[2.5, 3.0)	[0.28, 0.34)	6.47 ± 0.16	6.47 ± 0.16
[2.5, 3.0)	[0.34, 0.40)	3.87 ± 0.09	3.86 ± 0.09
[2.5, 3.0)	[0.40, 0.46)	2.21 ± 0.05	2.22 ± 0.05
[2.5, 3.0)	[0.46, 0.52)	1.236 ± 0.028	1.242 ± 0.028
[2.5, 3.0)	[0.52, 0.58)	0.680 ± 0.016	0.681 ± 0.016
[2.5, 3.0)	[0.58, 0.64)	0.358 ± 0.009	0.360 ± 0.009
[2.5, 3.0)	[0.64, 0.70)	0.186 ± 0.004	0.189 ± 0.005
[2.5, 3.0)	[0.70, 0.76)	0.0943 ± 0.0026	0.0967 ± 0.0033
[2.5, 3.0)	[0.76, 0.82)	0.0481 ± 0.0013	0.0487 ± 0.0015
[2.5, 3.0)	[0.82, 0.88)	$(24.3 \pm 1.0) \cdot 10^{-3}$	0.0251 ± 0.0012
[2.5, 3.0)	[0.88, 0.94)	$(12.3 \pm 0.5) \cdot 10^{-3}$	$(12.6 \pm 0.5) \cdot 10^{-3}$
[2.5, 3.0)	[0.94, 1.00)	$(6.04 \pm 0.34) \cdot 10^{-3}$	$(6.5 \pm 0.4) \cdot 10^{-3}$
[3.0, 3.5)	[-0.56, -0.50)	300 ± 17	299 ± 17
[3.0, 3.5)	[-0.50, -0.44)	268 ± 15	268 ± 15
[3.0, 3.5)	[-0.44, -0.38)	235 ± 13	234 ± 13
[3.0, 3.5)	[-0.38, -0.32)	202 ± 10	202 ± 10
[3.0, 3.5)	[-0.32, -0.26)	168 ± 7	168 ± 7
[3.0, 3.5)	[-0.26, -0.20)	137 ± 6	137 ± 6
[3.0, 3.5)	[-0.20, -0.14)	109 ± 4	109 ± 4
[3.0, 3.5)	[-0.14, -0.08)	84.6 ± 3.0	84.6 ± 3.0
[3.0, 3.5)	[-0.08, -0.02)	63.7 ± 2.0	63.7 ± 2.0
[3.0, 3.5)	[-0.02, 0.04)	46.5 ± 1.4	46.5 ± 1.4
[3.0, 3.5)	[0.04, 0.10)	32.8 ± 1.0	32.8 ± 1.0
[3.0, 3.5)	[0.10, 0.16)	22.2 ± 0.6	22.2 ± 0.6
[3.0, 3.5)	[0.16, 0.22)	14.45 ± 0.35	14.6 ± 0.4
[3.0, 3.5)	[0.22, 0.28)	9.30 ± 0.23	9.29 ± 0.23
[3.0, 3.5)	[0.28, 0.34)	5.71 ± 0.14	5.71 ± 0.14
[3.0, 3.5)	[0.34, 0.40)	3.39 ± 0.08	3.40 ± 0.08
[3.0, 3.5)	[0.40, 0.46)	1.98 ± 0.05	1.98 ± 0.05
[3.0, 3.5)	[0.46, 0.52)	1.103 ± 0.029	1.102 ± 0.027
[3.0, 3.5)	[0.52, 0.58)	0.597 ± 0.018	0.606 ± 0.016
[3.0, 3.5)	[0.58, 0.64)	0.314 ± 0.010	0.314 ± 0.008
[3.0, 3.5)	[0.64, 0.70)	0.163 ± 0.006	0.163 ± 0.005
[3.0, 3.5)	[0.70, 0.76)	0.0830 ± 0.0035	0.0821 ± 0.0029
[3.0, 3.5)	[0.76, 0.82)	0.0414 ± 0.0017	0.0422 ± 0.0017
[3.0, 3.5)	[0.82, 0.88)	0.0207 ± 0.0011	0.0214 ± 0.0011
[3.0, 3.5)	[0.88, 0.94)	$(10.1 \pm 0.7) \cdot 10^{-3}$	$(10.6 \pm 0.6) \cdot 10^{-3}$

η	$\log_{10}(p_T/(\text{GeV}/c))$	$(d^2\sigma/(d\eta dp_T))/(\text{mb}/(\text{GeV}/c))$	
		$q = -1$	$q = +1$
[3.0, 3.5)	[0.94, 1.00)	$(5.2 \pm 0.5) \cdot 10^{-3}$	$(5.1 \pm 0.4) \cdot 10^{-3}$
[3.5, 4.0)	[-0.74, -0.68)	334 ± 20	335 ± 20
[3.5, 4.0)	[-0.68, -0.62)	324 ± 19	324 ± 19
[3.5, 4.0)	[-0.62, -0.56)	307 ± 18	306 ± 18
[3.5, 4.0)	[-0.56, -0.50)	281 ± 16	280 ± 16
[3.5, 4.0)	[-0.50, -0.44)	252 ± 14	251 ± 14
[3.5, 4.0)	[-0.44, -0.38)	221 ± 11	221 ± 11
[3.5, 4.0)	[-0.38, -0.32)	191 ± 8	191 ± 8
[3.5, 4.0)	[-0.32, -0.26)	160 ± 6	161 ± 6
[3.5, 4.0)	[-0.26, -0.20)	131 ± 5	131 ± 5
[3.5, 4.0)	[-0.20, -0.14)	103 ± 4	103 ± 4
[3.5, 4.0)	[-0.14, -0.08)	78.5 ± 2.8	79.3 ± 2.8
[3.5, 4.0)	[-0.08, -0.02)	58.1 ± 1.8	58.6 ± 1.8
[3.5, 4.0)	[-0.02, 0.04)	41.7 ± 1.1	42.1 ± 1.2
[3.5, 4.0)	[0.04, 0.10)	29.0 ± 0.8	29.2 ± 0.8
[3.5, 4.0)	[0.10, 0.16)	19.5 ± 0.5	19.8 ± 0.5
[3.5, 4.0)	[0.16, 0.22)	12.80 ± 0.33	12.96 ± 0.34
[3.5, 4.0)	[0.22, 0.28)	8.15 ± 0.20	8.23 ± 0.21
[3.5, 4.0)	[0.28, 0.34)	5.02 ± 0.13	5.06 ± 0.12
[3.5, 4.0)	[0.34, 0.40)	2.96 ± 0.08	2.99 ± 0.07
[3.5, 4.0)	[0.40, 0.46)	1.70 ± 0.05	1.72 ± 0.05
[3.5, 4.0)	[0.46, 0.52)	0.938 ± 0.029	0.945 ± 0.026
[3.5, 4.0)	[0.52, 0.58)	0.498 ± 0.016	0.510 ± 0.015
[3.5, 4.0)	[0.58, 0.64)	0.258 ± 0.009	0.262 ± 0.008
[3.5, 4.0)	[0.64, 0.70)	0.132 ± 0.005	0.134 ± 0.005
[3.5, 4.0)	[0.70, 0.76)	0.0647 ± 0.0030	0.0675 ± 0.0030
[3.5, 4.0)	[0.76, 0.82)	0.0319 ± 0.0017	0.0337 ± 0.0018
[3.5, 4.0)	[0.82, 0.88)	0.0159 ± 0.0011	0.0168 ± 0.0010
[3.5, 4.0)	[0.88, 0.94)	$(8.0 \pm 0.7) \cdot 10^{-3}$	$(8.1 \pm 0.6) \cdot 10^{-3}$
[4.0, 4.5)	[-0.98, -0.92)	264 ± 28	260 ± 28
[4.0, 4.5)	[-0.92, -0.86)	285 ± 26	281 ± 25
[4.0, 4.5)	[-0.86, -0.80)	300 ± 23	297 ± 23
[4.0, 4.5)	[-0.80, -0.74)	306 ± 22	305 ± 21
[4.0, 4.5)	[-0.74, -0.68)	308 ± 19	306 ± 19
[4.0, 4.5)	[-0.68, -0.62)	301 ± 17	298 ± 17
[4.0, 4.5)	[-0.62, -0.56)	286 ± 14	284 ± 14
[4.0, 4.5)	[-0.56, -0.50)	265 ± 10	266 ± 10
[4.0, 4.5)	[-0.50, -0.44)	241 ± 8	241 ± 8
[4.0, 4.5)	[-0.44, -0.38)	213 ± 8	213 ± 8
[4.0, 4.5)	[-0.38, -0.32)	180 ± 6	180 ± 6
[4.0, 4.5)	[-0.32, -0.26)	150 ± 5	150 ± 5
[4.0, 4.5)	[-0.26, -0.20)	120.2 ± 3.3	121.0 ± 3.3
[4.0, 4.5)	[-0.20, -0.14)	93.5 ± 2.4	94.1 ± 2.4
[4.0, 4.5)	[-0.14, -0.08)	70.5 ± 1.8	71.0 ± 1.8

η	$\log_{10}(p_T/(\text{GeV}/c))$	$(d^2\sigma/(d\eta dp_T))/(\text{mb}/(\text{GeV}/c))$	
		$q = -1$	$q = +1$
[4.0, 4.5)	[-0.08, -0.02)	51.9 ± 1.3	52.4 ± 1.3
[4.0, 4.5)	[-0.02, 0.04)	37.2 ± 0.9	37.6 ± 0.9
[4.0, 4.5)	[0.04, 0.10)	25.7 ± 0.6	26.0 ± 0.6
[4.0, 4.5)	[0.10, 0.16)	17.3 ± 0.4	17.5 ± 0.4
[4.0, 4.5)	[0.16, 0.22)	11.25 ± 0.29	11.37 ± 0.28
[4.0, 4.5)	[0.22, 0.28)	7.03 ± 0.18	7.13 ± 0.18
[4.0, 4.5)	[0.28, 0.34)	4.26 ± 0.12	4.30 ± 0.11
[4.0, 4.5)	[0.34, 0.40)	2.47 ± 0.07	2.49 ± 0.06
[4.0, 4.5)	[0.40, 0.46)	1.36 ± 0.04	1.40 ± 0.04
[4.0, 4.5)	[0.46, 0.52)	0.741 ± 0.025	0.748 ± 0.021
[4.0, 4.5)	[0.52, 0.58)	0.386 ± 0.015	0.390 ± 0.014
[4.0, 4.5)	[0.58, 0.64)	0.195 ± 0.008	0.200 ± 0.007
[4.0, 4.5)	[0.64, 0.70)	0.096 ± 0.004	0.103 ± 0.004
[4.0, 4.5)	[0.70, 0.76)	0.0478 ± 0.0022	0.0523 ± 0.0024
[4.0, 4.5)	[0.76, 0.82)	0.0235 ± 0.0011	0.0253 ± 0.0013
[4.0, 4.5)	[0.82, 0.88)	$(11.3 \pm 0.6) \cdot 10^{-3}$	$(13.0 \pm 0.7) \cdot 10^{-3}$
[4.5, 4.8)	[-1.10, -1.04)	199 ± 28	195 ± 27
[4.5, 4.8)	[-1.04, -0.98)	228 ± 25	224 ± 24
[4.5, 4.8)	[-0.98, -0.92)	251 ± 23	249 ± 22
[4.5, 4.8)	[-0.92, -0.86)	272 ± 21	270 ± 20
[4.5, 4.8)	[-0.86, -0.80)	289 ± 20	284 ± 19
[4.5, 4.8)	[-0.80, -0.74)	299 ± 18	298 ± 17
[4.5, 4.8)	[-0.74, -0.68)	304 ± 13	303 ± 13
[4.5, 4.8)	[-0.68, -0.62)	300 ± 12	299 ± 12
[4.5, 4.8)	[-0.62, -0.56)	282 ± 11	282 ± 11
[4.5, 4.8)	[-0.56, -0.50)	258 ± 10	258 ± 10
[4.5, 4.8)	[-0.50, -0.44)	233 ± 8	233 ± 8
[4.5, 4.8)	[-0.44, -0.38)	203 ± 6	204 ± 6
[4.5, 4.8)	[-0.38, -0.32)	171 ± 4	172 ± 4
[4.5, 4.8)	[-0.32, -0.26)	142 ± 4	143 ± 4
[4.5, 4.8)	[-0.26, -0.20)	114.8 ± 2.9	115.9 ± 2.9
[4.5, 4.8)	[-0.20, -0.14)	89.3 ± 2.2	90.4 ± 2.2
[4.5, 4.8)	[-0.14, -0.08)	67.7 ± 1.6	68.4 ± 1.6
[4.5, 4.8)	[-0.08, -0.02)	49.6 ± 1.2	50.5 ± 1.2
[4.5, 4.8)	[-0.02, 0.04)	35.0 ± 0.8	35.7 ± 0.8
[4.5, 4.8)	[0.04, 0.10)	24.0 ± 0.6	24.4 ± 0.6
[4.5, 4.8)	[0.10, 0.16)	15.8 ± 0.4	16.1 ± 0.4
[4.5, 4.8)	[0.16, 0.22)	10.08 ± 0.25	10.34 ± 0.25
[4.5, 4.8)	[0.22, 0.28)	6.22 ± 0.16	6.35 ± 0.15
[4.5, 4.8)	[0.28, 0.34)	3.66 ± 0.12	3.72 ± 0.11
[4.5, 4.8)	[0.34, 0.40)	2.05 ± 0.08	2.12 ± 0.07
[4.5, 4.8)	[0.40, 0.46)	1.14 ± 0.04	1.18 ± 0.04
[4.5, 4.8)	[0.46, 0.52)	0.596 ± 0.023	0.631 ± 0.022
[4.5, 4.8)	[0.52, 0.58)	0.314 ± 0.013	0.328 ± 0.012

η	$\log_{10}(p_T/(\text{GeV}/c))$	$(d^2\sigma/(d\eta dp_T))/(\text{mb}/(\text{GeV}/c))$	
		$q = -1$	$q = +1$
[4.5, 4.8)	[0.58, 0.64)	0.152 ± 0.006	0.169 ± 0.006
[4.5, 4.8)	[0.64, 0.70)	0.075 ± 0.004	0.0854 ± 0.0033

B Correlation matrix of differential cross-section

The correlation matrix of the measured differential cross-section is shown in Fig. 12. The correlations are positive since the systematic uncertainties dominate and most of the systematic uncertainties are positively correlated between kinematic intervals and the two particle charges. The positive correlations between neighbouring p_T intervals are particularly large due to the correction of the tracking efficiency, which affects neighbouring

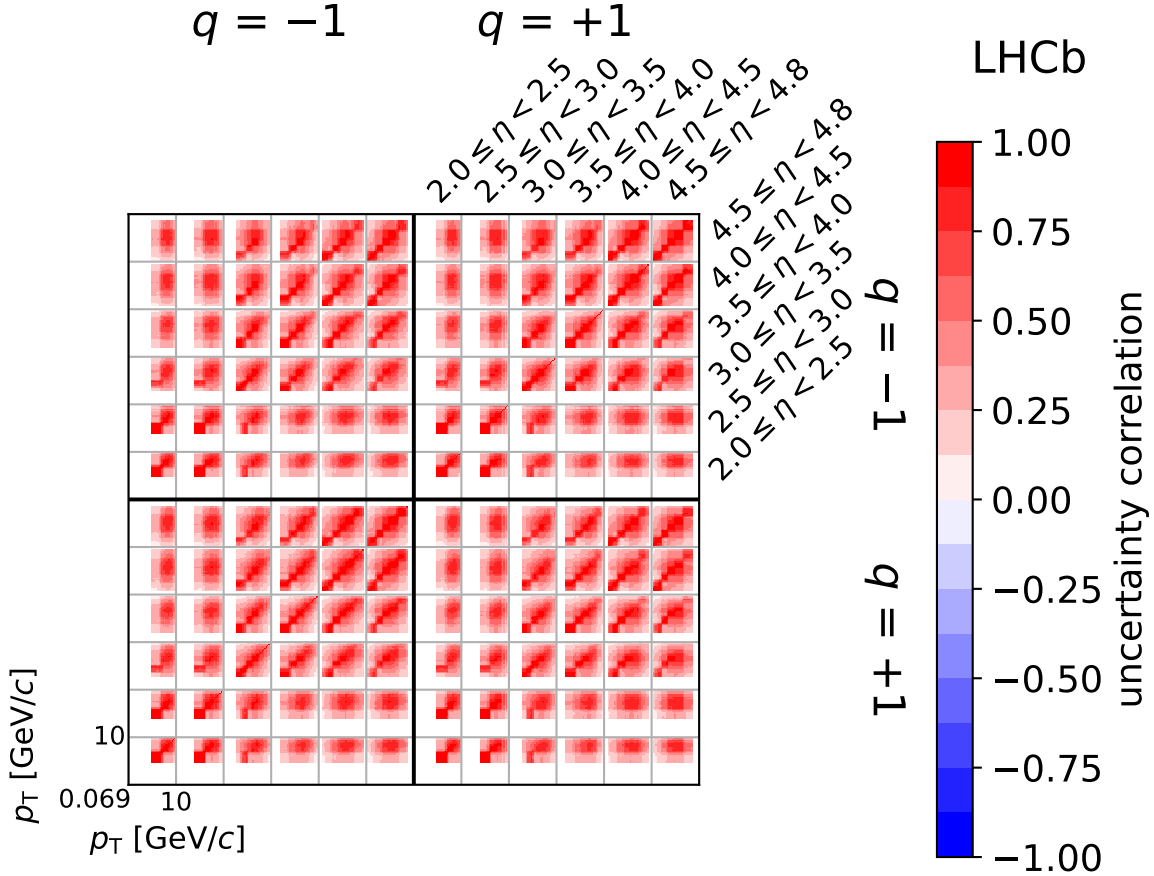


Figure 12: Correlation matrix for the uncertainties of the differential cross-section of prompt inclusive production of long-lived charged particles. The four large quadrants correspond to the correlations between negatively and positively charged particles. The 36 cells within each quadrant correspond to the η intervals. In each cell, the correlations of the p_T intervals are shown from low to high p_T in logarithmic intervals.

intervals in the same way. The numerical values of the correlation matrix are provided in machine-readable form at [link].

References

- [1] F. E. Low, *Model of the bare pomeron*, Phys. Rev. **D12** (1975) 163.
- [2] A. H. Mueller and H. Navelet, *An inclusive minijet cross section and the bare pomeron in QCD*, Nucl. Phys. **B282** (1987) 727.
- [3] N. N. Nikolaev and B. G. Zakharov, *Pomeron structure function and diffraction dissociation of virtual photons in perturbative QCD*, Z. Phys. **C53** (1992) 331.
- [4] K. Goulianos, *Universality of particle multiplicities*, 3rd Gleb Wataghin School on High Energy Phenomenology, 1994.
- [5] H. J. Drescher *et al.*, *Parton-based Gribov–Regge theory*, Phys. Rep. **350** (2001) 93, arXiv:hep-ph/0007198.
- [6] EAS-MSU, IceCube, KASCADE-Grande, NEVOD-DECOR, Pierre Auger, SUGAR, Telescope Array and Yakutsk EAS Array collaborations, H. P. Dembinski *et al.*, *Report on tests and measurements of hadronic interaction properties with air showers*, EPJ Web Conf. **210** (2019) 02004, arXiv:1902.08124.
- [7] H. P. Dembinski, *The Muon Puzzle in high-energy air showers*, Phys. Atom. Nuclei **82** (2019) 644.
- [8] Z. Citron *et al.*, *Future physics opportunities for high-density QCD at the LHC with heavy-ion and proton beams*, CERN Yellow Rep. Monogr. **7** (2019) 1159, arXiv:1812.06772.
- [9] S. Baur *et al.*, *Core-corona effect in hadron collisions and muon production in air showers*, arXiv:1902.09265.
- [10] J. Albrecht *et al.*, *The Muon Puzzle in cosmic-ray induced air showers and its connection to the Large Hadron Collider*, arXiv:2105.06148.
- [11] F. Riehn *et al.*, *Hadronic interaction model Sibyll 2.3d and extensive air showers*, Phys. Rev. **D102** (2020) 063002, arXiv:1912.03300.
- [12] S. Roesler, R. Engel, and J. Ranft, *The Monte Carlo event generator DPMJET-III*, arXiv:hep-ph/0012252.
- [13] A. Fedynitch, *Cascade equations and hadronic interactions at very high energies*, PhD thesis, Karlsruhe Institute of Technology, Karlsruhe, 2015, CERN-THESIS-2015-371.
- [14] T. Pierog *et al.*, *EPOS LHC: Test of collective hadronization with data measured at the CERN Large Hadron Collider*, Phys. Rev. **C92** (2015) 034906, arXiv:1306.0121.
- [15] S. Ostapchenko, *Monte Carlo treatment of hadronic interactions in enhanced pomeron scheme: QGSJET-II model*, Phys. Rev. **D83** (2011) 014018, arXiv:1010.1869.

- [16] LHCb collaboration, A. A. Alves Jr. *et al.*, *The LHCb detector at the LHC*, JINST **3** (2008) S08005.
- [17] LHCb collaboration, R. Aaij *et al.*, *LHCb detector performance*, Int. J. Mod. Phys. **A30** (2015) 1530022, arXiv:1412.6352.
- [18] T. Sjöstrand *et al.*, *An introduction to PYTHIA 8.2*, Comput. Phys. Commun. **191** (2015) 159, arXiv:1410.3012; T. Sjöstrand, S. Mrenna, and P. Skands, *PYTHIA 6.4 physics and manual*, JHEP **05** (2006) 026, arXiv:hep-ph/0603175.
- [19] I. Belyaev *et al.*, *Handling of the generation of primary events in Gauss, the LHCb simulation framework*, J. Phys. Conf. Ser. **331** (2011) 032047.
- [20] D. J. Lange, *The EvtGen particle decay simulation package*, Nucl. Instrum. Meth. **A462** (2001) 152.
- [21] N. Davidson, T. Przedzinski, and Z. Was, *PHOTOS interface in C++: Technical and physics documentation*, Comp. Phys. Comm. **199** (2016) 86, arXiv:1011.0937.
- [22] Geant4 collaboration, J. Allison *et al.*, *Geant4 developments and applications*, IEEE Trans. Nucl. Sci. **53** (2006) 270; Geant4 collaboration, S. Agostinelli *et al.*, *Geant4: A simulation toolkit*, Nucl. Instrum. Meth. **A506** (2003) 250.
- [23] M. Clemencic *et al.*, *The LHCb simulation application, Gauss: Design, evolution and experience*, J. Phys. Conf. Ser. **331** (2011) 032023.
- [24] ALICE collaboration, S. Acharya *et al.*, *The ALICE definition of primary particles*, ALICE-PUBLIC-2017-005, 2017.
- [25] M. De Cian, S. Farry, P. Seyfert, and S. Stahl, *Fast neural-net based fake track rejection in the LHCb reconstruction*, LHCb-PUB-2017-011, 2017.
- [26] LHCb collaboration, R. Aaij *et al.*, *Measurement of the track reconstruction efficiency at LHCb*, JINST **10** (2015) P02007, arXiv:1408.1251.
- [27] LHCb collaboration, R. Aaij *et al.*, *Measurement of prompt hadron production ratios in pp collisions at $\sqrt{s} = 0.9$ and 7 TeV*, Eur. Phys. J. **C72** (2012) 2168, arXiv:1206.5160.
- [28] R. Brun and F. Rademakers, *ROOT – An object oriented data analysis framework*, Nucl. Instrum. Meth. **A389** (1997) 81.
- [29] G. Corti *et al.*, *Software for the LHCb experiment*, IEEE Trans. Nucl. Sci. **53** (2006) 1323.
- [30] A. Tsaregorodtsev *et al.*, *DIRAC3: The new generation of the LHCb grid software*, J. Phys. Conf. Ser. **219** (2010) 062029.
- [31] J. D. Hunter, *Matplotlib: A 2D graphics environment*, Comput. Sci. Eng. **9** (2007) 90.
- [32] S. K. Lam *et al.*, *numba/numba: Version 0.52.0*, 2020. doi: 10.5281/zenodo.4343231.

- [33] C. R. Harris *et al.*, *Array programming with NumPy*, Nature **585** (2020) 357, [arXiv:2006.10256](#).
- [34] P. Virtanen *et al.*, *SciPy 1.0: Fundamental algorithms for scientific computing in Python*, Nat. Methods **17** (2020) 261, [arXiv:1907.10121](#).
- [35] J. Köster and S. Rahmann, *Snakemake—a scalable bioinformatics workflow engine*, Bioinformatics **28** (2012) 2520.
- [36] A. Meurer *et al.*, *SymPy: Symbolic computing in Python*, PeerJ Comput. Sci. **3** (2017) e103.
- [37] H. Schreiner *et al.*, *scikit-hep/boost-histogram: Version 0.12.0*, 2021. doi: 10.5281/zenodo.4476368.
- [38] H. Dembinski *et al.*, *scikit-hep/iminuit: v2.0.0*, 2020. doi: 10.5281/zenodo.4310361.
- [39] E. Rodrigues *et al.*, *scikit-hep/particle: Version 0.14.0*, 2020. doi: 10.5281/zenodo.4292256.
- [40] J. Pivarski *et al.*, *scikit-hep/uproot3: 3.14.2*, 2020. doi: 10.5281/zenodo.4321705.
- [41] E. Rodrigues *et al.*, *The Scikit HEP project – Overview and prospects*, EPJ Web Conf. **245** (2020) 06028, [arXiv:2007.03577](#).
- [42] M. Alexander *et al.*, *Mapping the material in the LHCb vertex locator using secondary hadronic interactions*, JINST **13** (2018) P06008, [arXiv:1803.07466](#).
- [43] R. Barlow, *Systematic errors: Facts and fictions*, [arXiv:hep-ex/0207026](#).
- [44] R. Barlow, *Extended maximum likelihood*, Nucl. Instrum. Meth. **A297** (1990) 496.
- [45] G. Bohm and G. Zech, *Statistics of weighted Poisson events and its applications*, Nucl. Instrum. Meth. **A748** (2014) 1, [arXiv:1309.1287](#).
- [46] F. N. Fritsch and R. E. Carlson, *Monotone piecewise cubic interpolation*, SIAM J. Numer. Anal. **17** (1980) 238.
- [47] ATLAS collaboration, M. Aaboud *et al.*, *Measurement of the inelastic proton-proton cross section at $\sqrt{s} = 13$ TeV with the ATLAS detector at the LHC*, Phys. Rev. Lett. **117** (2016) 182002, [arXiv:1606.02625](#).
- [48] LHCb collaboration, R. Aaij *et al.*, *Measurement of the inelastic pp cross-section at a centre-of-mass energy of $\sqrt{s} = 13$ TeV*, JHEP **06** (2018) 100, [arXiv:1803.10974](#).
- [49] TOTEM collaboration, G. Antchev *et al.*, *First measurement of elastic, inelastic and total cross-section at $\sqrt{s} = 13$ TeV by TOTEM and overview of cross-section data at LHC energies*, Eur. Phys. J. **C79** (2019) 103, [arXiv:1712.06153](#).
- [50] P. Skands, S. Carrazza, and J. Rojo, *Tuning PYTHIA 8.1: The Monash 2013 tune*, Eur. Phys. J. **C74** (2014) 3024, [arXiv:1404.5630](#).
- [51] R. Ulrich, T. Pierog, and C. Baus, *Cosmic ray Monte Carlo package, CRMC*, 2021. doi: 10.5281/zenodo.4558706.

LHCb collaboration

R. Aaij³², C. Abellán Beteta⁵⁰, T. Ackernley⁶⁰, B. Adeva⁴⁶, M. Adinolfi⁵⁴, H. Afsharnia⁹, C.A. Aidala⁸⁶, S. Aiola²⁵, Z. Ajaltouni⁹, S. Akar⁶⁵, L. Alasfar¹⁶, J. Albrecht¹⁵, F. Alessio⁴⁸, M. Alexander⁵⁹, A. Alfonso Alberro⁴⁵, Z. Aliouche⁶², G. Alkhazov³⁸, P. Alvarez Cartelle⁵⁵, S. Amato², Y. Amhis¹¹, L. An⁴⁸, L. Anderlini²², A. Andreianov³⁸, M. Andreotti²¹, F. Archilli¹⁷, A. Artamonov⁴⁴, M. Artuso⁶⁸, K. Arzymatov⁴², E. Aslanides¹⁰, M. Atzeni⁵⁰, B. Audurier¹², S. Bachmann¹⁷, M. Bachmayer⁴⁹, J.J. Back⁵⁶, P. Baladron Rodriguez⁴⁶, V. Balagura¹², W. Baldini²¹, J. Baptista Leite¹, R.J. Barlow⁶², S. Barsuk¹¹, W. Barter⁶¹, M. Bartolini²⁴, F. Baryshnikov⁸³, J.M. Basels¹⁴, G. Bassi²⁹, B. Batsukh⁶⁸, A. Battig¹⁵, A. Bay⁴⁹, M. Becker¹⁵, F. Bedeschi²⁹, I. Bediaga¹, A. Beiter⁶⁸, V. Belavin⁴², S. Belin²⁷, V. Bellee⁴⁹, K. Belous⁴⁴, I. Belov⁴⁰, I. Belyaev⁴¹, G. Bencivenni²³, E. Ben-Haim¹³, A. Berezhnoy⁴⁰, R. Bernet⁵⁰, D. Berninghoff¹⁷, H.C. Bernstein⁶⁸, C. Bertella⁴⁸, A. Bertolin²⁸, C. Betancourt⁵⁰, F. Betti⁴⁸, Ia. Bezshyiko⁵⁰, S. Bhasin⁵⁴, J. Bhom³⁵, L. Bian⁷³, M.S. Bieker¹⁵, S. Bifani⁵³, P. Billoir¹³, M. Birch⁶¹, F.C.R. Bishop⁵⁵, A. Bitadze⁶², A. Bizzeti^{22,k}, M. Bjørn⁶³, M.P. Blago⁴⁸, T. Blake⁵⁶, F. Blanc⁴⁹, S. Blusk⁶⁸, D. Bobulska⁵⁹, J.A. Boelhauve¹⁵, O. Boente Garcia⁴⁶, T. Boettcher⁶⁵, A. Boldyrev⁸², A. Bondar⁴³, N. Bondar^{38,48}, S. Borghi⁶², M. Borisyak⁴², M. Borsato¹⁷, J.T. Borsuk³⁵, S.A. Bouchiba⁴⁹, T.J.V. Bowcock⁶⁰, A. Boyer⁴⁸, C. Bozzi²¹, M.J. Bradley⁶¹, S. Braun⁶⁶, A. Brea Rodriguez⁴⁶, M. Brodski⁴⁸, J. Brodzicka³⁵, A. Brossa Gonzalo⁵⁶, D. Brundu²⁷, A. Buonauro⁵⁰, C. Burr⁴⁸, A. Bursche⁷², A. Butkevich³⁹, J.S. Butter³², J. Buytaert⁴⁸, W. Byczynski⁴⁸, S. Cadeddu²⁷, H. Cai⁷³, R. Calabrese^{21,f}, L. Calefice^{15,13}, L. Calero Diaz²³, S. Cali²³, R. Calladine⁵³, M. Calvi^{26,j}, M. Calvo Gomez⁸⁵, P. Camargo Magalhaes⁵⁴, P. Campana²³, A.F. Campoverde Quezada⁶, S. Capelli^{26,j}, L. Capriotti^{20,d}, A. Carbone^{20,d}, G. Carboni³¹, R. Cardinale²⁴, A. Cardini²⁷, I. Carli⁴, P. Carniti^{26,j}, L. Carus¹⁴, K. Carvalho Akiba³², A. Casais Vidal⁴⁶, G. Casse⁶⁰, M. Cattaneo⁴⁸, G. Cavallero⁴⁸, S. Celani⁴⁹, J. Cerasoli¹⁰, A.J. Chadwick⁶⁰, M.G. Chapman⁵⁴, M. Charles¹³, Ph. Charpentier⁴⁸, G. Chatzikonstantinidis⁵³, C.A. Chavez Barajas⁶⁰, M. Chefdeville⁸, C. Chen³, S. Chen⁴, A. Chernov³⁵, V. Chobanova⁴⁶, S. Cholak⁴⁹, M. Chruszcz³⁵, A. Chubykin³⁸, V. Chulikov³⁸, P. Ciambrone²³, M.F. Cicala⁵⁶, X. Cid Vidal⁴⁶, G. Ciezarek⁴⁸, P.E.L. Clarke⁵⁸, M. Clemencic⁴⁸, H.V. Cliff⁵⁵, J. Closier⁴⁸, J.L. Cobbedick⁶², V. Coco⁴⁸, J.A.B. Coelho¹¹, J. Cogan¹⁰, E. Cogneras⁹, L. Cojocariu³⁷, P. Collins⁴⁸, T. Colombo⁴⁸, L. Congedo^{19,c}, A. Contu²⁷, N. Cooke⁵³, G. Coombs⁵⁹, G. Corti⁴⁸, C.M. Costa Sobral⁵⁶, B. Couturier⁴⁸, D.C. Craik⁶⁴, J. Crkovská⁶⁷, M. Cruz Torres¹, R. Currie⁵⁸, C.L. Da Silva⁶⁷, S. Dadabaev⁸³, E. Dall'Occo¹⁵, J. Dalseno⁴⁶, C. D'Ambrosio⁴⁸, A. Danilina⁴¹, P. d'Argent⁴⁸, A. Davis⁶², O. De Aguiar Francisco⁶², K. De Bruyn⁷⁹, S. De Capua⁶², M. De Cian⁴⁹, J.M. De Miranda¹, L. De Paula², M. De Serio^{19,c}, D. De Simone⁵⁰, P. De Simone²³, J.A. de Vries⁸⁰, C.T. Dean⁶⁷, D. Decamp⁸, L. Del Buono¹³, B. Delaney⁵⁵, H.-P. Dembinski¹⁵, A. Dendek³⁴, V. Denysenko⁵⁰, D. Derkach⁸², O. Deschamps⁹, F. Desse¹¹, F. Dettori^{27,e}, B. Dey⁷⁷, A. Di Cicco²³, P. Di Nezza²³, S. Didenko⁸³, L. Dieste Maronas⁴⁶, H. Dijkstra⁴⁸, V. Dobishuk⁵², A.M. Donohoe¹⁸, F. Dordei²⁷, A.C. dos Reis¹, L. Douglas⁵⁹, A. Dovbnya⁵¹, A.G. Downes⁸, K. Dreimaniš⁶⁰, M.W. Dudek³⁵, L. Dufour⁴⁸, V. Duk⁷⁸, P. Durante⁴⁸, J.M. Durham⁶⁷, D. Dutta⁶², A. Dziurda³⁵, A. Dzyuba³⁸, S. Easo⁵⁷, U. Egede⁶⁹, V. Egorychev⁴¹, S. Eidelman^{43,v}, S. Eisenhardt⁵⁸, S. Ek-In⁴⁹, L. Eklund^{59,w}, S. Ely⁶⁸, A. Ene³⁷, E. Epple⁶⁷, S. Escher¹⁴, J. Eschle⁵⁰, S. Esen¹³, T. Evans⁴⁸, A. Falabella²⁰, J. Fan³, Y. Fan⁶, B. Fang⁷³, S. Farry⁶⁰, D. Fazzini^{26,j}, M. Féo⁴⁸, A. Fernandez Prieto⁴⁶, J.M. Fernandez-tenllado Arribas⁴⁵, A.D. Fernez⁶⁶, F. Ferrari^{20,d}, L. Ferreira Lopes⁴⁹, F. Ferreira Rodrigues², S. Ferreres Sole³², M. Ferrillo⁵⁰, M. Ferro-Luzzi⁴⁸, S. Filippov³⁹, R.A. Fini¹⁹, M. Fiorini^{21,f}, M. Firlej³⁴, K.M. Fischer⁶³, D.S. Fitzgerald⁸⁶, C. Fitzpatrick⁶², T. Fiutowski³⁴, A. Fkiaras⁴⁸, F. Fleuret¹², M. Fontana¹³, F. Fontanelli^{24,h}, R. Forty⁴⁸, V. Franco Lima⁶⁰, M. Franco Sevilla⁶⁶, M. Frank⁴⁸, E. Franzoso²¹, G. Frau¹⁷, C. Frei⁴⁸, D.A. Friday⁵⁹, J. Fu²⁵, Q. Fuehring¹⁵, W. Funk⁴⁸,

E. Gabriel³², T. Gaintseva⁴², A. Gallas Torreira⁴⁶, D. Galli^{20,d}, S. Gambetta^{58,48}, Y. Gan³,
 M. Gandelman², P. Gandini²⁵, Y. Gao⁵, M. Garau²⁷, L.M. Garcia Martin⁵⁶,
 P. Garcia Moreno⁴⁵, J. García Pardiñas^{26,j}, B. Garcia Plana⁴⁶, F.A. Garcia Rosales¹²,
 L. Garrido⁴⁵, C. Gaspar⁴⁸, R.E. Geertsema³², D. Gerick¹⁷, L.L. Gerken¹⁵, E. Gersabeck⁶²,
 M. Gersabeck⁶², T. Gershon⁵⁶, D. Gerstel¹⁰, Ph. Ghez⁸, V. Gibson⁵⁵, H.K. Giemza³⁶,
 M. Giovannetti^{23,p}, A. Gioventù⁴⁶, P. Gironella Gironell⁴⁵, L. Giubega³⁷, C. Giugliano^{21,f,48},
 K. Gizdov⁵⁸, E.L. Gkougkousis⁴⁸, V.V. Gligorov¹³, C. Göbel⁷⁰, E. Golobardes⁸⁵, D. Golubkov⁴¹,
 A. Golutvin^{61,83}, A. Gomes^{1,a}, S. Gomez Fernandez⁴⁵, F. Goncalves Abrantes⁶³, M. Goncerz³⁵,
 G. Gong³, P. Gorbounov⁴¹, I.V. Gorelov⁴⁰, C. Gotti²⁶, E. Govorkova⁴⁸, J.P. Grabowski¹⁷,
 T. Grammatico¹³, L.A. Granado Cardoso⁴⁸, E. Graugés⁴⁵, E. Graverini⁴⁹, G. Graziani²²,
 A. Grecu³⁷, L.M. Greeven³², P. Griffith^{21,f}, L. Grillo⁶², S. Gromov⁸³, B.R. Gruberg Cazon⁶³,
 C. Gu³, M. Guarise²¹, P. A. Günther¹⁷, E. Gushchin³⁹, A. Guth¹⁴, Y. Guz⁴⁴, T. Gys⁴⁸,
 T. Hadavizadeh⁶⁹, G. Haefeli⁴⁹, C. Haen⁴⁸, J. Haimberger⁴⁸, T. Halewood-leagas⁶⁰,
 P.M. Hamilton⁶⁶, J.P. Hammerich⁶⁰, Q. Han⁷, X. Han¹⁷, T.H. Hancock⁶³,
 S. Hansmann-Menzemer¹⁷, N. Harnew⁶³, T. Harrison⁶⁰, C. Hasse⁴⁸, M. Hatch⁴⁸, J. He^{6,b},
 M. Hecker⁶¹, K. Heijhoff³², K. Heinicke¹⁵, A.M. Hennequin⁴⁸, K. Hennessy⁶⁰, L. Henry⁴⁸,
 J. Heuel¹⁴, A. Hicheur², D. Hill⁴⁹, M. Hilton⁶², S.E. Hollitt¹⁵, J. Hu¹⁷, J. Hu⁷², W. Hu⁷,
 X. Hu³, W. Huang⁶, X. Huang⁷³, W. Hulsbergen³², R.J. Hunter⁵⁶, M. Hushchyn⁸²,
 D. Hutchcroft⁶⁰, D. Hynds³², P. Ibis¹⁵, M. Idzik³⁴, D. Ilin³⁸, P. Ilten⁶⁵, A. Inglessi³⁸,
 A. Ishteev⁸³, K. Ivshin³⁸, R. Jacobsson⁴⁸, S. Jakobsen⁴⁸, E. Jans³², B.K. Jashal⁴⁷,
 A. Jawahery⁶⁶, V. Jevtic¹⁵, M. Jezabek³⁵, F. Jiang³, M. John⁶³, D. Johnson⁴⁸, C.R. Jones⁵⁵,
 T.P. Jones⁵⁶, B. Jost⁴⁸, N. Jurik⁴⁸, S. Kandybei⁵¹, Y. Kang³, M. Karacson⁴⁸, M. Karpov⁸²,
 F. Keizer⁴⁸, M. Kenzie⁵⁶, T. Ketel³³, B. Khanji¹⁵, A. Kharisova⁸⁴, S. Kholodenko⁴⁴, T. Kirn¹⁴,
 V.S. Kirsebom⁴⁹, O. Kitouni⁶⁴, S. Klaver³², K. Klimaszewski³⁶, S. Koliiev⁵², A. Kondybayeva⁸³,
 A. Konoplyannikov⁴¹, P. Kopciwicz³⁴, R. Kopecna¹⁷, P. Koppenburg³², M. Korolev⁴⁰,
 I. Kostiuk^{32,52}, O. Kot⁵², S. Kotriakhova^{21,38}, P. Kravchenko³⁸, L. Kravchuk³⁹,
 R.D. Krawczyk⁴⁸, M. Kreps⁵⁶, F. Kress⁶¹, S. Kretzschmar¹⁴, P. Krokovny^{43,v}, W. Krupa³⁴,
 W. Krzemien³⁶, W. Kucewicz^{35,t}, M. Kucharczyk³⁵, V. Kudryavtsev^{43,v}, H.S. Kuindersma^{32,33},
 G.J. Kunde⁶⁷, T. Kvaratskheliya⁴¹, D. Lacarrere⁴⁸, G. Lafferty⁶², A. Lai²⁷, A. Lampis²⁷,
 D. Lancierini⁵⁰, J.J. Lane⁶², R. Lane⁵⁴, G. Lanfranchi²³, C. Langenbruch¹⁴, J. Langer¹⁵,
 O. Lantwin⁵⁰, T. Latham⁵⁶, F. Lazzari^{29,q}, R. Le Gac¹⁰, S.H. Lee⁸⁶, R. Lefèvre⁹, A. Leflat⁴⁰,
 S. Legotin⁸³, O. Leroy¹⁰, T. Lesiak³⁵, B. Leverington¹⁷, H. Li⁷², L. Li⁶³, P. Li¹⁷, S. Li⁷, Y. Li⁴,
 Y. Li⁴, Z. Li⁶⁸, X. Liang⁶⁸, T. Lin⁶¹, R. Lindner⁴⁸, V. Lisovskyi¹⁵, R. Litvinov²⁷, G. Liu⁷²,
 H. Liu⁶, S. Liu⁴, A. Loi²⁷, J. Lomba Castro⁴⁶, I. Longstaff⁵⁹, J.H. Lopes², G.H. Lovell⁵⁵, Y. Lu⁴,
 D. Lucchesi^{28,l}, S. Luchuk³⁹, M. Lucio Martinez³², V. Lukashenko^{32,52}, Y. Luo³, A. Lupato⁶²,
 E. Luppi^{21,f}, O. Lupton⁵⁶, A. Lusiani^{29,m}, X. Lyu⁶, L. Ma⁴, R. Ma⁶, S. Maccolini^{20,d},
 F. Machefert¹¹, F. Maciuc³⁷, V. Macko⁴⁹, P. Mackowiak¹⁵, S. Maddrell-Mander⁵⁴,
 O. Madejczyk³⁴, L.R. Madhan Mohan⁵⁴, O. Maev³⁸, A. Maevskiy⁸², D. Maisuzenko³⁸,
 M.W. Majewski³⁴, J.J. Malczewski³⁵, S. Malde⁶³, B. Malecki⁴⁸, A. Malinin⁸¹, T. Maltsev^{43,v},
 H. Malygina¹⁷, G. Manca^{27,e}, G. Mancinelli¹⁰, D. Manuzzi^{20,d}, D. Marangotto^{25,i}, J. Maratas^{9,s},
 J.F. Marchand⁸, U. Marconi²⁰, S. Mariani^{22,g}, C. Marin Benito⁴⁸, M. Marinangeli⁴⁹, J. Marks¹⁷,
 A.M. Marshall⁵⁴, P.J. Marshall⁶⁰, G. Martellotti³⁰, L. Martinazzoli^{48,j}, M. Martinelli^{26,j},
 D. Martinez Santos⁴⁶, F. Martinez Vidal⁴⁷, A. Massafferri¹, M. Materok¹⁴, R. Matev⁴⁸,
 A. Mathad⁵⁰, Z. Mathe⁴⁸, V. Matiunin⁴¹, C. Matteuzzi²⁶, K.R. Mattioli⁸⁶, A. Mauri³²,
 E. Maurice¹², J. Mauricio⁴⁵, M. Mazurek⁴⁸, M. McCann⁶¹, L. McConnell¹⁸, T.H. Mcgrath⁶²,
 A. McNab⁶², R. McNulty¹⁸, J.V. Mead⁶⁰, B. Meadows⁶⁵, G. Meier¹⁵, N. Meinert⁷⁶,
 D. Melnychuk³⁶, S. Meloni^{26,j}, M. Merk^{32,80}, A. Merli²⁵, L. Meyer Garcia², M. Mikhasenko⁴⁸,
 D.A. Milanese⁷⁴, E. Millard⁵⁶, M. Milovanovic⁴⁸, M.-N. Minard⁸, A. Minotti²¹, L. Minzoni^{21,f},
 S.E. Mitchell⁵⁸, B. Mitreska⁶², D.S. Mitzel⁴⁸, A. Mödden¹⁵, R.A. Mohammed⁶³, R.D. Moise⁶¹,
 T. Mombächer⁴⁶, I.A. Monroy⁷⁴, S. Monteil⁹, M. Morandin²⁸, G. Morello²³, M.J. Morello^{29,m},

J. Moron³⁴, A.B. Morris⁷⁵, A.G. Morris⁵⁶, R. Mountain⁶⁸, H. Mu³, F. Muheim^{58,48},
 M. Mulder⁴⁸, D. Müller⁴⁸, K. Müller⁵⁰, C.H. Murphy⁶³, D. Murray⁶², P. Muzzetto^{27,48},
 P. Naik⁵⁴, T. Nakada⁴⁹, R. Nandakumar⁵⁷, T. Nanut⁴⁹, I. Nasteva², M. Needham⁵⁸, I. Neri²¹,
 N. Neri^{25,i}, S. Neubert⁷⁵, N. Neufeld⁴⁸, R. Newcombe⁶¹, T.D. Nguyen⁴⁹, C. Nguyen-Mau^{49,x},
 E.M. Niel¹¹, S. Nieswand¹⁴, N. Nikitin⁴⁰, N.S. Nolte⁶⁴, C. Normand⁸, C. Nunez⁸⁶,
 A. Oblakowska-Mucha³⁴, V. Obraztsov⁴⁴, D.P. O'Hanlon⁵⁴, R. Oldeman^{27,e}, M.E. Olivares⁶⁸,
 C.J.G. Onderwater⁷⁹, R.H. O'neil⁵⁸, A. Ossowska³⁵, J.M. Otalora Goicochea²,
 T. Ovsianikova⁴¹, P. Owen⁵⁰, A. Oyanguren⁴⁷, B. Pagare⁵⁶, P.R. Pais⁴⁸, T. Pajero⁶³,
 A. Palano¹⁹, M. Palutan²³, Y. Pan⁶², G. Panshin⁸⁴, A. Papanestis⁵⁷, M. Pappagallo^{19,c},
 L.L. Pappalardo^{21,f}, C. Pappenheimer⁶⁵, W. Parker⁶⁶, C. Parkes⁶², C.J. Parkinson⁴⁶,
 B. Passalacqua²¹, G. Passaleva²², A. Pastore¹⁹, M. Patel⁶¹, C. Patrignani^{20,d}, C.J. Pawley⁸⁰,
 A. Pearce⁴⁸, A. Pellegrino³², M. Pepe Altarelli⁴⁸, S. Perazzini²⁰, D. Pereima⁴¹, P. Perret⁹,
 M. Petric^{59,48}, K. Petridis⁵⁴, A. Petrolini^{24,h}, A. Petrov⁸¹, S. Petrucci⁵⁸, M. Petruzzo²⁵,
 T.T.H. Pham⁶⁸, A. Philippov⁴², L. Pica^{29,m}, M. Piccini⁷⁸, B. Pietrzyk⁸, G. Pietrzyk⁴⁹,
 M. Pili⁶³, D. Pinci³⁰, F. Pisani⁴⁸, Resmi P.K¹⁰, V. Placinta³⁷, J. Plews⁵³, M. Plo Casasus⁴⁶,
 F. Polci¹³, M. Poli Lener²³, M. Poliakova⁶⁸, A. Poluektov¹⁰, N. Polukhina^{83,u}, I. Polyakov⁶⁸,
 E. Polcarpo², G.J. Pomery⁵⁴, S. Ponce⁴⁸, D. Popov^{6,48}, S. Popov⁴², S. Poslavskii⁴⁴,
 K. Prasanth³⁵, L. Promberger⁴⁸, C. Prouve⁴⁶, V. Pugatch⁵², H. Pullen⁶³, G. Punzi^{29,n}, H. Qi³,
 W. Qian⁶, J. Qin⁶, N. Qin³, R. Quagliani¹³, B. Quintana⁸, N.V. Raab¹⁸, R.I. Rabadan Trejo¹⁰,
 B. Rachwal³⁴, J.H. Rademacker⁵⁴, M. Rama²⁹, M. Ramos Pernas⁵⁶, M.S. Rangel²,
 F. Ratnikov^{42,82}, G. Raven³³, M. Reboud⁸, F. Redi⁴⁹, F. Reiss⁶², C. Remon Alepuz⁴⁷, Z. Ren³,
 V. Renaudin⁶³, R. Ribatti²⁹, S. Ricciardi⁵⁷, K. Rinnert⁶⁰, P. Robbe¹¹, G. Robertson⁵⁸,
 A.B. Rodrigues⁴⁹, E. Rodrigues⁶⁰, J.A. Rodriguez Lopez⁷⁴, A. Rollings⁶³, P. Roloff⁴⁸,
 V. Romanovskiy⁴⁴, M. Romero Lamas⁴⁶, A. Romero Vidal⁴⁶, J.D. Roth⁸⁶, M. Rotondo²³,
 M.S. Rudolph⁶⁸, T. Ruf⁴⁸, J. Ruiz Vidal⁴⁷, A. Ryzhikov⁸², J. Ryzka³⁴, J.J. Saborido Silva⁴⁶,
 N. Sagidova³⁸, N. Sahoo⁵⁶, B. Saitta^{27,e}, M. Salomoni⁴⁸, D. Sanchez Gonzalo⁴⁵,
 C. Sanchez Gras³², R. Santacesaria³⁰, C. Santamarina Rios⁴⁶, M. Santimaria²³,
 E. Santovetti^{31,p}, D. Saranin⁸³, G. Sarpis⁶², M. Sarpis⁷⁵, A. Sarti³⁰, C. Satriano^{30,o}, A. Satta³¹,
 M. Saur¹⁵, D. Savrina^{41,40}, H. Sazak⁹, L.G. Scantlebury Smead⁶³, A. Scarabotto¹³, S. Schael¹⁴,
 M. Schiller⁵⁹, H. Schindler⁴⁸, M. Schmelling¹⁶, B. Schmidt⁴⁸, O. Schneider⁴⁹, A. Schopper⁴⁸,
 M. Schubiger³², S. Schulte⁴⁹, M.H. Schune¹¹, R. Schwemmer⁴⁸, B. Sciascia²³, S. Sellam⁴⁶,
 A. Semennikov⁴¹, M. Senghi Soares³³, A. Sergi²⁴, N. Serra⁵⁰, L. Sestini²⁸, A. Seuthe¹⁵,
 P. Seyfert⁴⁸, Y. Shang⁵, D.M. Shangase⁸⁶, M. Shapkin⁴⁴, I. Shchemerov⁸³, L. Shchutka⁴⁹,
 T. Shears⁶⁰, L. Shekhtman^{43,v}, Z. Shen⁵, V. Shevchenko⁸¹, E.B. Shields^{26,j}, E. Shmanin⁸³,
 J.D. Shupperd⁶⁸, B.G. Siddi²¹, R. Silva Coutinho⁵⁰, G. Simi²⁸, S. Simone^{19,c}, N. Skidmore⁶²,
 T. Skwarnicki⁶⁸, M.W. Slater⁵³, I. Slazyk^{21,f}, J.C. Smallwood⁶³, J.G. Smeaton⁵⁵,
 A. Smetkina⁴¹, E. Smith⁵⁰, M. Smith⁶¹, A. Snoch³², M. Soares²⁰, L. Soares Lavra⁹,
 M.D. Sokoloff⁶⁵, F.J.P. Soler⁵⁹, A. Solovev³⁸, I. Solovyev³⁸, F.L. Souza De Almeida²,
 B. Souza De Paula², B. Spaan¹⁵, E. Spadaro Norella^{25,i}, P. Spradlin⁵⁹, F. Stagni⁴⁸, M. Stahl⁶⁵,
 S. Stahl⁴⁸, P. Steffko⁴⁹, O. Steinkamp^{50,83}, O. Stenyakin⁴⁴, H. Stevens¹⁵, S. Stone⁶⁸,
 M.E. Stramaglia⁴⁹, M. Straticiu³⁷, D. Strelakina⁸³, F. Suljik⁶³, J. Sun²⁷, L. Sun⁷³, Y. Sun⁶⁶,
 P. Svihra⁶², P.N. Swallow⁵³, K. Swientek³⁴, A. Szabelski³⁶, T. Szumlak³⁴, M. Szymanski⁴⁸,
 S. Taneja⁶², A.R. Tanner⁵⁴, A. Terentev⁸³, F. Teubert⁴⁸, E. Thomas⁴⁸, K.A. Thomson⁶⁰,
 V. Tisserand⁹, S. T'Jampens⁸, M. Tobin⁴, L. Tomassetti^{21,f}, D. Torres Machado¹, D.Y. Tou¹³,
 M.T. Tran⁴⁹, E. Trifonova⁸³, C. Trippel⁴⁹, G. Tuci^{29,n}, A. Tully⁴⁹, N. Tuning^{32,48}, A. Ukleja³⁶,
 D.J. Unverzagt¹⁷, E. Ursov⁸³, A. Usachov³², A. Ustyuzhanin^{42,82}, U. Uwer¹⁷, A. Vagner⁸⁴,
 V. Vagnoni²⁰, A. Valassi⁴⁸, G. Valenti²⁰, N. Valls Canudas⁸⁵, M. van Beuzekom³²,
 M. Van Dijk⁴⁹, E. van Herwijnen⁸³, C.B. Van Hulse¹⁸, M. van Veghel⁷⁹, R. Vazquez Gomez⁴⁶,
 P. Vazquez Regueiro⁴⁶, C. Vázquez Sierra⁴⁸, S. Vecchi²¹, J.J. Velthuis⁵⁴, M. Veltri^{22,r},
 A. Venkateswaran⁶⁸, M. Veronesi³², M. Vesterinen⁵⁶, D. Vieira⁶⁵, M. Vieites Diaz⁴⁹,

H. Viemann⁷⁶, X. Vilasis-Cardona⁸⁵, E. Vilella Figueras⁶⁰, A. Villa²⁰, P. Vincent¹³,
D. Vom Bruch¹⁰, A. Vorobyev³⁸, V. Vorobyev^{43,v}, N. Voropaev³⁸, K. Vos⁸⁰, R. Waldi¹⁷,
J. Walsh²⁹, C. Wang¹⁷, J. Wang⁵, J. Wang⁴, J. Wang³, J. Wang⁷³, M. Wang³, R. Wang⁵⁴,
Y. Wang⁷, Z. Wang⁵⁰, Z. Wang³, H.M. Wark⁶⁰, N.K. Watson⁵³, S.G. Weber¹³, D. Websdale⁶¹,
C. Weisser⁶⁴, B.D.C. Westhenry⁵⁴, D.J. White⁶², M. Whitehead⁵⁴, D. Wiedner¹⁵,
G. Wilkinson⁶³, M. Wilkinson⁶⁸, I. Williams⁵⁵, M. Williams⁶⁴, M.R.J. Williams⁵⁸,
F.F. Wilson⁵⁷, W. Wislicki³⁶, M. Witek³⁵, L. Witola¹⁷, G. Wormser¹¹, S.A. Wotton⁵⁵, H. Wu⁶⁸,
K. Wyllie⁴⁸, Z. Xiang⁶, D. Xiao⁷, Y. Xie⁷, A. Xu⁵, J. Xu⁶, L. Xu³, M. Xu⁷, Q. Xu⁶, Z. Xu⁵,
Z. Xu⁶, D. Yang³, S. Yang⁶, Y. Yang⁶, Z. Yang³, Z. Yang⁶⁶, Y. Yao⁶⁸, L.E. Yeomans⁶⁰, H. Yin⁷,
J. Yu⁷¹, X. Yuan⁶⁸, O. Yushchenko⁴⁴, E. Zaffaroni⁴⁹, M. Zavertyaev^{16,u}, M. Zdybal³⁵,
O. Zenaiev⁴⁸, M. Zeng³, D. Zhang⁷, L. Zhang³, S. Zhang⁵, Y. Zhang⁵, Y. Zhang⁶³,
A. Zharkova⁸³, A. Zhelezov¹⁷, Y. Zheng⁶, X. Zhou⁶, Y. Zhou⁶, X. Zhu³, Z. Zhu⁶, V. Zhukov^{14,40},
J.B. Zonneveld⁵⁸, Q. Zou⁴, S. Zucchelli^{20,d}, D. Zuliani²⁸, G. Zunica⁶².

¹Centro Brasileiro de Pesquisas Físicas (CBPF), Rio de Janeiro, Brazil

²Universidade Federal do Rio de Janeiro (UFRJ), Rio de Janeiro, Brazil

³Center for High Energy Physics, Tsinghua University, Beijing, China

⁴Institute Of High Energy Physics (IHEP), Beijing, China

⁵School of Physics State Key Laboratory of Nuclear Physics and Technology, Peking University, Beijing, China

⁶University of Chinese Academy of Sciences, Beijing, China

⁷Institute of Particle Physics, Central China Normal University, Wuhan, Hubei, China

⁸Univ. Savoie Mont Blanc, CNRS, IN2P3-LAPP, Annecy, France

⁹Université Clermont Auvergne, CNRS/IN2P3, LPC, Clermont-Ferrand, France

¹⁰Aix Marseille Univ, CNRS/IN2P3, CPPM, Marseille, France

¹¹Université Paris-Saclay, CNRS/IN2P3, IJCLab, Orsay, France

¹²Laboratoire Leprince-Ringuet, CNRS/IN2P3, Ecole Polytechnique, Institut Polytechnique de Paris, Palaiseau, France

¹³LPNHE, Sorbonne Université, Paris Diderot Sorbonne Paris Cité, CNRS/IN2P3, Paris, France

¹⁴I. Physikalisches Institut, RWTH Aachen University, Aachen, Germany

¹⁵Fakultät Physik, Technische Universität Dortmund, Dortmund, Germany

¹⁶Max-Planck-Institut für Kernphysik (MPIK), Heidelberg, Germany

¹⁷Physikalisches Institut, Ruprecht-Karls-Universität Heidelberg, Heidelberg, Germany

¹⁸School of Physics, University College Dublin, Dublin, Ireland

¹⁹INFN Sezione di Bari, Bari, Italy

²⁰INFN Sezione di Bologna, Bologna, Italy

²¹INFN Sezione di Ferrara, Ferrara, Italy

²²INFN Sezione di Firenze, Firenze, Italy

²³INFN Laboratori Nazionali di Frascati, Frascati, Italy

²⁴INFN Sezione di Genova, Genova, Italy

²⁵INFN Sezione di Milano, Milano, Italy

²⁶INFN Sezione di Milano-Bicocca, Milano, Italy

²⁷INFN Sezione di Cagliari, Monserrato, Italy

²⁸Università degli Studi di Padova, Università e INFN, Padova, Padova, Italy

²⁹INFN Sezione di Pisa, Pisa, Italy

³⁰INFN Sezione di Roma La Sapienza, Roma, Italy

³¹INFN Sezione di Roma Tor Vergata, Roma, Italy

³²Nikhef National Institute for Subatomic Physics, Amsterdam, Netherlands

³³Nikhef National Institute for Subatomic Physics and VU University Amsterdam, Amsterdam, Netherlands

³⁴AGH - University of Science and Technology, Faculty of Physics and Applied Computer Science, Kraków, Poland

³⁵Henryk Niewodniczanski Institute of Nuclear Physics Polish Academy of Sciences, Kraków, Poland

³⁶National Center for Nuclear Research (NCBJ), Warsaw, Poland

³⁷Horia Hulubei National Institute of Physics and Nuclear Engineering, Bucharest-Magurele, Romania

- ³⁸ Petersburg Nuclear Physics Institute NRC Kurchatov Institute (PNPI NRC KI), Gatchina, Russia
- ³⁹ Institute for Nuclear Research of the Russian Academy of Sciences (INR RAS), Moscow, Russia
- ⁴⁰ Institute of Nuclear Physics, Moscow State University (SINP MSU), Moscow, Russia
- ⁴¹ Institute of Theoretical and Experimental Physics NRC Kurchatov Institute (ITEP NRC KI), Moscow, Russia
- ⁴² Yandex School of Data Analysis, Moscow, Russia
- ⁴³ Budker Institute of Nuclear Physics (SB RAS), Novosibirsk, Russia
- ⁴⁴ Institute for High Energy Physics NRC Kurchatov Institute (IHEP NRC KI), Protvino, Russia, Protvino, Russia
- ⁴⁵ ICCUB, Universitat de Barcelona, Barcelona, Spain
- ⁴⁶ Instituto Galego de Física de Altas Enerxías (IGFAE), Universidade de Santiago de Compostela, Santiago de Compostela, Spain
- ⁴⁷ Instituto de Física Corpuscular, Centro Mixto Universidad de Valencia - CSIC, Valencia, Spain
- ⁴⁸ European Organization for Nuclear Research (CERN), Geneva, Switzerland
- ⁴⁹ Institute of Physics, Ecole Polytechnique Fédérale de Lausanne (EPFL), Lausanne, Switzerland
- ⁵⁰ Physik-Institut, Universität Zürich, Zürich, Switzerland
- ⁵¹ NSC Kharkiv Institute of Physics and Technology (NSC KIPT), Kharkiv, Ukraine
- ⁵² Institute for Nuclear Research of the National Academy of Sciences (KINR), Kyiv, Ukraine
- ⁵³ University of Birmingham, Birmingham, United Kingdom
- ⁵⁴ H.H. Wills Physics Laboratory, University of Bristol, Bristol, United Kingdom
- ⁵⁵ Cavendish Laboratory, University of Cambridge, Cambridge, United Kingdom
- ⁵⁶ Department of Physics, University of Warwick, Coventry, United Kingdom
- ⁵⁷ STFC Rutherford Appleton Laboratory, Didcot, United Kingdom
- ⁵⁸ School of Physics and Astronomy, University of Edinburgh, Edinburgh, United Kingdom
- ⁵⁹ School of Physics and Astronomy, University of Glasgow, Glasgow, United Kingdom
- ⁶⁰ Oliver Lodge Laboratory, University of Liverpool, Liverpool, United Kingdom
- ⁶¹ Imperial College London, London, United Kingdom
- ⁶² Department of Physics and Astronomy, University of Manchester, Manchester, United Kingdom
- ⁶³ Department of Physics, University of Oxford, Oxford, United Kingdom
- ⁶⁴ Massachusetts Institute of Technology, Cambridge, MA, United States
- ⁶⁵ University of Cincinnati, Cincinnati, OH, United States
- ⁶⁶ University of Maryland, College Park, MD, United States
- ⁶⁷ Los Alamos National Laboratory (LANL), Los Alamos, United States
- ⁶⁸ Syracuse University, Syracuse, NY, United States
- ⁶⁹ School of Physics and Astronomy, Monash University, Melbourne, Australia, associated to ⁵⁶
- ⁷⁰ Pontifícia Universidade Católica do Rio de Janeiro (PUC-Rio), Rio de Janeiro, Brazil, associated to ²
- ⁷¹ Physics and Micro Electronic College, Hunan University, Changsha City, China, associated to ⁷
- ⁷² Guangdong Provincial Key Laboratory of Nuclear Science, Guangdong-Hong Kong Joint Laboratory of Quantum Matter, Institute of Quantum Matter, South China Normal University, Guangzhou, China, associated to ³
- ⁷³ School of Physics and Technology, Wuhan University, Wuhan, China, associated to ³
- ⁷⁴ Departamento de Física, Universidad Nacional de Colombia, Bogota, Colombia, associated to ¹³
- ⁷⁵ Universität Bonn - Helmholtz-Institut für Strahlen und Kernphysik, Bonn, Germany, associated to ¹⁷
- ⁷⁶ Institut für Physik, Universität Rostock, Rostock, Germany, associated to ¹⁷
- ⁷⁷ Eotvos Lorand University, Budapest, Hungary, associated to ⁴⁸
- ⁷⁸ INFN Sezione di Perugia, Perugia, Italy, associated to ²¹
- ⁷⁹ Van Swinderen Institute, University of Groningen, Groningen, Netherlands, associated to ³²
- ⁸⁰ Universiteit Maastricht, Maastricht, Netherlands, associated to ³²
- ⁸¹ National Research Centre Kurchatov Institute, Moscow, Russia, associated to ⁴¹
- ⁸² National Research University Higher School of Economics, Moscow, Russia, associated to ⁴²
- ⁸³ National University of Science and Technology "MISIS", Moscow, Russia, associated to ⁴¹
- ⁸⁴ National Research Tomsk Polytechnic University, Tomsk, Russia, associated to ⁴¹
- ⁸⁵ DS4DS, La Salle, Universitat Ramon Llull, Barcelona, Spain, associated to ⁴⁵
- ⁸⁶ University of Michigan, Ann Arbor, United States, associated to ⁶⁸

^a Universidade Federal do Triângulo Mineiro (UFTM), Uberaba-MG, Brazil

^b Hangzhou Institute for Advanced Study, UCAS, Hangzhou, China

- ^c *Università di Bari, Bari, Italy*
- ^d *Università di Bologna, Bologna, Italy*
- ^e *Università di Cagliari, Cagliari, Italy*
- ^f *Università di Ferrara, Ferrara, Italy*
- ^g *Università di Firenze, Firenze, Italy*
- ^h *Università di Genova, Genova, Italy*
- ⁱ *Università degli Studi di Milano, Milano, Italy*
- ^j *Università di Milano Bicocca, Milano, Italy*
- ^k *Università di Modena e Reggio Emilia, Modena, Italy*
- ^l *Università di Padova, Padova, Italy*
- ^m *Scuola Normale Superiore, Pisa, Italy*
- ⁿ *Università di Pisa, Pisa, Italy*
- ^o *Università della Basilicata, Potenza, Italy*
- ^p *Università di Roma Tor Vergata, Roma, Italy*
- ^q *Università di Siena, Siena, Italy*
- ^r *Università di Urbino, Urbino, Italy*
- ^s *MSU - Iligan Institute of Technology (MSU-IIT), Iligan, Philippines*
- ^t *AGH - University of Science and Technology, Faculty of Computer Science, Electronics and Telecommunications, Kraków, Poland*
- ^u *P.N. Lebedev Physical Institute, Russian Academy of Science (LPI RAS), Moscow, Russia*
- ^v *Novosibirsk State University, Novosibirsk, Russia*
- ^w *Department of Physics and Astronomy, Uppsala University, Uppsala, Sweden*
- ^x *Hanoi University of Science, Hanoi, Vietnam*